Sea Ice Rheology Experiment (SIREx), Part II: Evaluating simulated linear kinematic features in high-resolution sea-ice simulations

Nils Christian Hutter[1], Amélie Bouchat[2], Frederic Dupont[3], Dmitry S Dukhovskoy[4], Nikolay V. Koldunov[5], Younjoo J Lee[6], Jean-Francois Lemieux[7], Camille Lique[8], Martin Losch[5], Wieslaw Maslowski[6], Paul G. Myers[9], Einar Örn Ólason[10], Pierre Rampal[11], Till Andreas Soya Rasmussen[12], Claude Talandier[13], Bruno Tremblay[2], and Qiang Wang[5]

[1]Alfred Wegener Institute, Helmholtz Centre for Polar and Marine Research
[2]McGill University
[3]Environment Canada
[4]Florida State University
[5]Alfred Wegener Institute for Polar and Marine Research
[6]Naval Postgraduate School
[7]Environnement et Changement Climatique Canada
[8]Laboratoire d'Océanographie Physique et Spatiale
[9]University of Alberta
[10]Nansen Environmental and Remote Sensing Center
[11]Institut des Geosciences de l'Environnement
[12]Danish Meteorological Institute
[13]LPO, CNRS-IFREMER-IRD-UBO

November 22, 2022

Abstract

Simulating sea-ice drift and deformation in the Arctic Ocean is still a challenge because of the multi-scale interaction of sea-ice floes that compose the Arctic sea ice cover. The Sea Ice Rheology Experiment (SIREx) is a model intercomparison project formed within the Forum of Arctic Modeling and Observational Synthesis (FAMOS) to collect and design skill metrics to evaluate different recently suggested approaches for modeling linear kinematic features (LKFs) and provide guidance for modeling small-scale deformation. In this contribution, spatial and temporal properties of LKFs are assessed in 36 simulations of state-of-the-art sea ice models and compared to deformation features derived from RADARSAT Geophysical Processor System (RGPS). All simulations produce LKFs, but only very few models realistically simulate at least some statistics of LKF properties such as densities, lengths, or growth rates. All SIREx models overestimate the angle of fracture between conjugate pairs of LKFs and LKF lifetimes pointing to inaccurate model physics. The temporal and spatial resolution of a simulation and the spatial resolution of atmospheric forcing affect simulated LKFs as much as the model's sea ice rheology and numerics. Only in very high resolution simulations ([?]2\,km) the concentration and thickness anomalies along LKFs are large enough to affect air-ice-ocean interaction processes.

Sea Ice Rheology Experiment (SIREx), Part II: Evaluating simulated linear kinematic features in high-resolution sea-ice simulations

Nils Hutter[1], Amélie Bouchat[2], Frédéric Dupont[3], Dmitry Dukhovskoy[4], Nikolay Koldunov[1], Younjoo Lee[5], Jean-François Lemieux[6], Camille Lique[7], Martin Losch[1], Wieslaw Maslowski[5], Paul G. Myers[8], Einar Ólason[9], Pierre Rampal[10], Till Rasmussen[11], Claude Talandier[7], Bruno Tremblay[2], Qiang Wang[1]

[1]Alfred-Wegener-Institut, Helmholtz Zentrum für Polar- und Meeresforschung, Bremerhaven, Germany.
[2]Department of Atmospheric and Oceanic Sciences, McGill University,Montréal, QC, Canada.
[3]Service Météorologique Canadien, Environnement et Changement Climatique Canada, Dorval, Qc, Canada
[4]Center for Ocean-Atmospheric Prediction Studies, Florida State University, Tallahassee, FL, USA
[5]Department of Oceanography, Naval Postgraduate School, Monterey, California, USA
[6]Recherche en Prévision Numérique Environnementale, Environnement et Changement Climatique Canada, Dorval, Qc, Canada
[7]University of Brest, CNRS, IRD, Ifremer, Laboratoire d'Océanographie Physique et Spatiale (LOPS), IUEM, Brest, France
[8]Department of Earth and Atmospheric Sciences, University of Alberta, Edmonton, Alberta, Canada
[9]Nansen Environmental and Remote Sensing Centre, and Bjerknes Centre for Climate Research, Bergen, Norway
[10]Institut de Géophysique de l'Environnement, CNRS, Grenoble, France
[11]Danish Meteorological Institute, Copenhagen, Denmark

Key Points:

- there are multiple methods to simulate leads and pressure ridges in sea ice models
- resolved LKFs are affected by spatial and temporal resolution of model grid and atmospheric forcing and rheology
- Skill metrics are designed and applied to evaluate linear kinematic features in the model intercomparison

Corresponding author: Nils Hutter, `nils.hutter@awi.de`

Abstract

Simulating sea-ice drift and deformation in the Arctic Ocean is still a challenge because of the multi-scale interaction of sea-ice floes that compose the Arctic sea ice cover. The Sea Ice Rheology Experiment (SIREx) is a model intercomparison project formed within the Forum of Arctic Modeling and Observational Synthesis (FAMOS) to collect and design skill metrics to evaluate different recently suggested approaches for modeling linear kinematic features (LKFs) and provide guidance for modeling small-scale deformation. In this contribution, spatial and temporal properties of LKFs are assessed in 36 simulations of state-of-the-art sea ice models and compared to deformation features derived from RADARSAT Geophysical Processor System (RGPS). All simulations produce LKFs, but only very few models realistically simulate at least some statistics of LKF properties such as densities, lengths, or growth rates. All SIREx models overestimate the angle of fracture between conjugate pairs of LKFs and LKF lifetimes pointing to inaccurate model physics. The temporal and spatial resolution of a simulation and the spatial resolution of atmospheric forcing affect simulated LKFs as much as the model's sea ice rheology and numerics. Only in very high resolution simulations ($\leq$2 km) the concentration and thickness anomalies along LKFs are large enough to affect air-ice-ocean interaction processes.

Plain Language Summary

Winds and ocean currents constantly push and break the ice cover of the Arctic ocean into many floes. The distribution of ice floes and open water between them is important for climate research, as ice reflects more light and energy and open water takes up more heat from the atmosphere leading to warmer oceans. Current climate models cannot simulate sea ice as individual floes. Various methods have been proposed to represent the deformation and fracture of ice in sea-ice models. The Sea Ice Rheology Experiment (SIREx) compares these different approaches and assesses the deformation of sea ice in 36 simulations. In this study, we identify and track deformation features in the ice cover and explore specific spacial and temporal properties, for example, if there are specific regions where the ice is more fractured than in others, or how long individual deformation events take. These spacial and regional properties are compared to satellite observations to find out how realistic the simulations are. From this comparison, we can learn how to improve sea-ice models for more realistic simulations of sea-ice deformation.

1 Introduction

Continuous and omnipresent deformation turns the Arctic sea ice cover into a mosaic of ice floes. The deformations concentrate in narrow bands along floe boundaries, where the ice breaks and ridges in divergent, convergent, and especially shear motions. Recently, the focus of the sea-ice modeling community on thermodynamics and large-scale circulation of sea ice has extended to resolving these small-scale deformation processes in sea-ice dynamics. High resolution applications as well as changes to the model physics describing the material properties of ice allow to explicitly resolve deformation that is localized in narrow lines consisting of segments of leads and pressure ridges. These elongated deformation bands are referred to as Linear Kinematic Features (LKFs).

Leads and pressure ridges represent only a small fraction of the large scale ice cover, but their presence changes the interaction of sea ice with the ocean and atmosphere in the Arctic climate system substantially. The opening of the ice cover in a lead results in intensified heat and humidity exchange between the ocean and atmosphere, resulting in ice growth, brine rejection in the ocean, and convective processes in both the ocean and atmosphere (e.g. Lüpkes et al., 2008). The sea ice piled along pressure ridges determine the regional surface roughness which in turn affects the atmospheric and oceanic boundary layer circulation, snow distribution, and drag forces acting on the ice (e.g. Martin et al., 2016). Currently, coarse resolution Global Climate Models resolve very poorly discontinuities in the pack ice (or LKFs). Instead, the effects of leads on heat and freshwater fluxes and ultimately on the Arctic climate are modeled by sub-grid scale parameterizations such as fractional ice cover variables. To directly simulate these processes and to provide a more detailed picture of the complex Arctic climate system, we need sea-ice models that explicitly resolve LKFs. A dynamical framework with strongly localized sea ice deformation is the first step towards a realistic representation of leads and pressure ridges in continuum sea ice models that will be used in climate simulations for the foreseeable future (Hunke et al., 2020; Blockley et al., 2020).

Various adjustments have been suggested to improve the representation of LKFs and to resolve leads in continuum sea-ice models: (1) increasing the model resolution to a horizontal grid spacing smaller than 5 km (e.g. Q. Wang et al., 2016; Hutter et al., 2018), (2) modifying the yield curve (e.g. Bouchat & Tremblay, 2017), and (3) introducing new rheological frameworks (e.g. Elasto Brittle (EB), Maxwell Elasto Brittle (MEB), Girard et al., 2011; Bouillon & Rampal, 2015; Dansereau et al., 2016). All three approaches require the convergence of the dynamics solver to ensure accurate solutions (Lemieux & Tremblay, 2009; Losch et al., 2014; Q. Wang et al., 2016; Koldunov et al., 2019). In most cases, the observed localization of deformation rates have been assessed with multifractal scaling analyses to describe the LKF representation in space and time (Marsan et al., 2004; Rampal et al., 2016; Bouchat & Tremblay, 2017; Hutter et al., 2018; Rampal et al., 2019). The scaling analysis does not allow unambiguous discrimination between different rheologies in comparison to satellite observations (Rampal et al., 2016; Bouchat & Tremblay, 2017; Hutter et al., 2018). This raises two questions: First, if all rheologies perform similarly well, are the scaling analyses a sufficient tool to investigate differences between the rheologies? Second, scaling analyses give insights into the underlying material properties and deformation physics, but is this relevant for LKF properties on climate scales (e.g. LKF size, opening times, etc.)? It is plausible that explicit simulations of the interaction of atmosphere, ice, and ocean associated with sea ice leads may require a realistic spatial and temporal distribution of LKFs (e.g. Ólason et al., 2020). Hutter and Losch (2020) showed that scaling analyses alone cannot evaluate this aspect in their simulations with the viscous-plastic (VP) rheology (Hibler, 1979). However, using a combination of scaling analysis and statistics from automated LKF detection algorithms (Linow & Dierking, 2017; Hutter et al., 2019) allows for a comprehensive evaluation of LKFs.

In 2017, the sea-ice modeling working group of the Forum of Arctic Modeling and Observational Synthesis (FAMOS, Proshutinsky et al., 2020) launched the Sea Ice Rheology Experiment (SIREx) model intercomparison project with two aims: (1) to extend the current research on simulating small-scale sea ice deformation to additional modeling frameworks, namely all rheologies used in the sea-ice modeling on climate scales, and (2) to develop, compare, and combine new and existing evaluation metrics to gauge the realism of the simulated features. In total, 10 international groups participated with 36 simulations from 11 different models. The contributed simulations cover all rheologies commonly used in Pan-Arctic sea ice simulations with continuum models (viscous plastic or its elastic-viscous-plastic variation — (E)VP, elastic anisotropic plastic — EAP, and, Maxwell elasto brittle — MEB), as well as a large range of model resolutions (1 km to 15 km), different atmospheric forcing (reanalysis with different spatial and temporal resolution as well as interactively coupled atmospheric models), and different parameterisations with different effects on the ice strength (different number of ice thickness categories or ITD classes and modified yield curve parameters). The analysis of this suite of simulations is structured in two parts: Part I (Bouchat et al., 2020) focuses on the conventional scaling metrics to study the heterogeneity and intermittency in the simulated deformation fields. Combined with new uncertainty estimates (Bouchat & Tremblay, 2019), this analysis offers insights into the physical properties of the simulated ice deformation that forms LKFs. In SIREx Part II — the subject of this paper — we make use of automated detection and tracking algorithms (Hutter et al., 2019) to study the spatial and temporal distribution and characteristics of LKFs, for example, densities, lengths, and lifetimes. This analysis provides a comprehensive description of simulated deformation features and allows for the evaluation of LKF properties that are highly relevant for interaction processes at the air-ice-ocean interface.

The objective of this paper is to evaluate the spatial and temporal properties of simulated deformation features in all SIREx models with satellite observations. We use detection and tracking algorithms to extract LKFs in simulated deformation fields and compare them to the RGPS LKF data set (Hutter et al., 2019). The comparison is made for the two winters (JFM) 1997 and 2008. The results of this comparison are interpreted in light of the different model parameters and parameterisations (for example, rheology or spatial resolution) to assess the impact and importance of individual parameters on the quality of resolved LKFs. We link our feature-based evaluation to the scaling analysis of SIREx Part I (Bouchat et al., 2020) and to an analysis of sea-ice thickness and concentration anomalies along resolved LKFs. This forms an in-depth comparison of different dynamical modeling frameworks for sea ice and their capabilities for simulating localized deformation along floe boundaries. A special focus of this intercomparison project, besides the insights for sea-ice rheology and model development, is to provide guidance for users of sea-ice models in the context of coupled climate simulations in the Arctic.

2 Data

In this section, we introduce the different model simulations and the observational data-set that we use for the comparison.

2.1 RGPS LKF data

The RGPS data set is a high spatial resolution data set of sea-ice deformation that is often used for model evaluation (e.g. Spreen et al., 2016; Bouchat & Tremblay, 2017; Rampal et al., 2019; Hutter & Losch, 2020). From the RGPS deformation data set, an LKF data set was generated (Section 3.1, Hutter et al., 2019; Hutter et al., 2019) that contains 165 000 detected and 36 000 tracked LKFs in the winters 1996/97 to 2007/08. For this study, we subsample the RGPS LKF data set to the two SIREx winters (January, February, and March in 1997 and 2008) for the model evaluation. The remaining winters (JFM 1998 to 2007) are used to estimate the interannual variability of LKF statistics in the RGPS data set.

2.2 Model data

Eleven models contributed to the second part of SIREx with a total of 22 simulations and 36 simulated winters. The participating models cover a broad variety in terms of rheology, spatial grid resolution, temporal and spatial resolution of atmospheric forcing, ITD classes, and grid type (structured vs. unstructured, Lagrangian vs. Eulerian). Some important details of the model simulations are summarized in Table 1; for further information we refer to the specific references provided in Table 1. Note that the MERCATOR model participating in SIREx Part I does not participate in our analysis. For all simulations sea-ice drift, concentration, and thickness were provided for at least one SIREx winter (14 of the simulations cover both years and 8 simulations cover either 1997 or 2008). The SIREx winters have been chosen based on availability of existing model output and to be representative of a large period of sea ice retreat. Most of the model output is provided as daily mean fields, only some groups provided daily snapshots. The PDFs of deformation rates are robust to the choice of output diagnostic (snapshots vs. daily mean, results not shown). For this reason, we process both types of output in the same way in the processing steps outlined in Section 3.2.

Table 1. Key parameters of high-resolution runs participating in SIREx adapted from Bouchat et al. (2020). The run numbers (Run no.) correspond to Bouchat et al. (2020). We use the following abbreviations: grid types are E: Eulerian, L:Lagrangian, U: Unstructured; Ice strength parameters are P^*: compressive strength parameter (kPa), T^*: isotropic tensile strength parameter (kPa), e: ellipse aspect ratio, C_f: frictional energy dissipation parameter; ITD # is the number of ice-thickness categories in the ice thickness distribution; and nb. is the number of iteration performed to solve the dynamical equations. The grid spacing is given by the mean horizontal grid spacing within the Arctic Ocean. For unstructured grids it refers to the mean node spacing.

Model/Configuration (Group) (Label)	Year	Grid spacing, Time step	Grid	Rheology (nb. it)	Ice Strength Parameters	ITD #	Atm. Forcing (Δx, Δt)	Reference
MITgcm (AWI)								
MITgcm (2km, ITD)	1997, 2008	2 km, 120s	E	VP (LSR)	$P^*, e = 22.64$, 2.0	5	JRA55 (∼60 km, 3 hr)	(Hutter & Losch, 2020)
MITgcm (2km, e=1,↓P)	1997, 2008	"	"	"	$P^*, e = 9.6$, 1.0	2	"	-
MITgcm (2km, e=0.7,↓P)	1997, 2008	"	"	"	$P^*, e = 9.6$, 0.7	2	"	-
MITgcm (2km)	1997, 2008	"	"	"	$P^*, e = 22.64$, 2.0	"	"	(Hutter & Losch, 2020)
MITgcm (4.5km)	2008	4.5 km, 240s	"	"	"	"	ERA-Interim (∼80 km, 6 hr)	(Mohammadi-Aragh et al., 2018)
McGill-SIM (McGill)								
McGill (e=2)	1997	10 km, 3600s	E	VP (JFNK)	$P^*, e = 27.5$, 2.0	2	NCEP/NCAR (2.5°, 6 hr)	(Bouchat & Tremblay, 2017)
McGill (e=1,↓P)	1997	"	"	"	$P^*, e = 13.8$, 1.0	"	"	"
McGill (e=0.7,↓P)	1997	"	"	"	$P^*, e = 9.6$, 0.7	"	"	"
McGill (e=1,↑S)	1997	"	"	"	$P^*, e = 27.5$, 1.0	"	"	"
NEMO-LIM3/CREG4 (IFREMER)								
IFREMER (e=2)	1997, 2008	12.4 km, 720s	E	EVP (120)	$P^*, e = 20.0$, 2.0	5	DFS 5.2 (∼ 0.7°, 3 hr)	(Muilwijk et al., 2019)
IFREMER (e=1)	1997, 2008	"	"	"	$P^*, e = 13.8$, 1.0	"	"	"
HYCOM-CICE4 (FSU)								
HYCOM-CICE (FSU)	1997, 2008	3.6 km, 360s	E	EVP (120)	C_f,e= 19,2.0	5	CFSR/CFSv2 (∼ 38 km, 1 hr)	(Dukhovskoy et al., 2019)
HYCOM-CICE4 (DMI)								
DMI	2008	9.7 km, 180s	E	EVP (120)	$P^*, e = 27.5$, 2.0	5	ERA-Interim (80 km, 3 hr)	(Madsen et al., 2016)
NEMO-LIM2/ANHA12 (U.Alberta)								
ANHA (4km)	2008	4.1 km, 180s	E	EVP (120)	$P^*, e = 23.4$, 2.0	2	CGRF (∼35 km, 1 hr)	(Hu et al., 2018)
NEMO-LIM2/ANHA4 (U.Alberta)								
ANHA (12km)	1997, 2008	12.4 km, 1080s	E	EVP (150)	$P^*, e = 23.4$, 2.0	2	CORE (∼200 km, 6 hr)	(Courtois et al., 2017)
RIOPS/CREG12-H08 (ECCC)								
RIOPS	2008	4.1 km, 180s	E	EVP (900)	$P^*, e = 27.5$, 1.5 $T^* = 1.375$	10	CGRF (∼35 km, 3 hr)	(Dupont et al., 2015)
FESOM (AWI)								
FESOM	1997, 2008	5.1 km, 600s	U	EVP (800)	$P^*, e = 27.5$, 2.0	2	NCEP/NCAR (∼ 1.9°, 24 hr)	(Q. Wang et al., 2016)
FESOM2 (AWI)								
FESOM2	1997, 2008	1 km, 180s	U	mEVP (400)	$P^*, e = 27.5$, 2.0	2	JRA55 (∼60 km, 3 hr)	(Q. Wang et al., 2020)
RASM - Fully Coupled (NPS)								
RASM-WRF (EVP)	1997, 2008	9.1 km, 1200s	E	EVP (600)	$C_f, e = 21.3$, 2.0	5	WRF Model (50 km, 20 min)	-
RASM-WRF (EAP)	1997, 2008	9.1 km, 1200s	E	EAP (600)	"	"	"	-
RASM-CORE2 (NPS)								
RASM-CORE2 (EAP)	1997, 2008	9.1 km, 1200s	E	EAP (120)	$C_f, e = 21.3$, 2.0	5	CORE2 (∼ 110 km, 24 hr)	-
neXtSIM - V1(2018) (NERSC)								
neXtSIM	1997, 2008	10 km, 200s	L	MEB	$T^*, P^* = 21$, 75	3	CFSR/CFSv2 (0.5° version, 6 hr)	(Rampal et al., 2019)

3 Methods

In this section, we describe how the LKF detection and tracking algorithms are applied and what sampling we use for the model data.

3.1 LKF detection and tracking algorithms

At the core of our feature-based evaluation are data-sets of LKFs. These are derived from sea ice deformation fields from satellite observations and simulation data by automatic feature detection and tracking. The automatic feature detection and tracking algorithms are described in Hutter (2019). A brief summary follows.

From the original map of deformation, a binary map of LKF pixels is created that have significantly higher deformation rates than their immediate neighborhood. Then, this binary map is divided into short segments of neighboring LKF pixels. Finally, segments are reconnected based on a probability function that describes their distance, the orientation relative to each other, and the difference in deformation rate.

The tracking algorithm uses drift information between pairs of subsequent LKF fields to advect the LKFs of the first field. The advected features are then compared to the LKFs in the second field. Tracked LKFs are identified based on the degree of overlap between advected LKFs of the first field and detected LKFs of the second field.

3.2 Detection and tracking of LKFs in the model data

The LKF detection and tracking algorithms require the data to be on a regular grid (Hutter et al., 2019). The output fields from the unstructured grid models were interpolated onto regular grids with similar spatial resolution (FESOM to the grid of MITgcm 4.5km, FESOM2 to the grid of MITgcm 2km, and neXtSIM to a grid with 10km grid spacing in Polar Stereographic projection). All other model output was processed on the native model grids.

We adapt the filtering technique of the LKF detection algorithm to account for the fact that the model and RGPS data do not have the same sampling frequencies (3-day for the RGPS and 1-day for the models). We mimic the 3-day sampling of RGPS by combining three daily deformation fields in the following way: (1) total deformation rates are computed by finite differences from the daily drift output. (2) Pixels are flagged as LKF pixels in each daily total deformation field with a difference of Gaussian (DoG) filter in the following way: We scale the original kernel sizes of the DoG filter (radii $r_1 = 1\,\text{pixel}$ and $r_2 = 5\,\text{pixel}$) by a factor $f = \frac{1}{2} + \frac{1}{2}\frac{\Delta x_{rgps}}{\Delta x_{model}}$ to take into account the fact that very high resolution simulations can have finer scale features than RGPS data. Pixels are then flagged as LKF when their total deformation exceeds the average deformation rate in the immediate neighborhood (averaged over a radius of $62.5\,km$) by $d_{LKF} = 0.01\,\text{day}^{-1}$. This threshold is determined to be fine enough to filter all LKFs, but still high enough to prevent spurious detection of noise in the deformation fields that is caused by a lower accuracy of the solution. Only the neXtSIM simulation contains LKFs lower than this threshold such that we use a threshold of $d_{LKF} = 0.002\,\text{day}^{-1}$ for this simulation. (3) The three daily deformation fields are combined into one binary map where a specific pixel is flagged as LKF if any of the three daily fields are flagged as LKF at this pixel position. (4) A morphological thinning algorithm is applied to the combined binary map to reduce all LKFs to a width of 1 pixel. By applying the morphological thinning algorithm explicitly after combining the daily LKF maps, we ensure that LKFs that move within 3 days are not detected more than once. A detailed discussion of the comparability of the RGPS LKF data set and the derived model LKF data sets with respect to spatial and temporal resolution is included in Appendix A.

The detection routines (segment detection and reconnection of Hutter et al., 2019) are applied to the combined and thinned binary maps. Both algorithms utilize optimized parameters for the RGPS data set (Table 1 in Hutter et al., 2019), with the minimal length of LKFs scaled by the corresponding model resolution. The simulated ice drift fields are also used, besides for deriving deformation, to advect the LKFs over three day intervals (between the 3-daily records) for the tracking algorithm. In the following, we use the optimized tracking algorithm parameters for the RGPS data set (Table 2 in Hutter et al., 2019).

3.3 Principles of the model-observation comparison

The RGPS data set covers most of the Arctic Ocean, but the coverage varies in time depending on the available SAR imagery. Gaps in the deformation data can split long LKFs into multiple smaller LKFs or inhibit tracking of LKFs. This affects derived LKF statistics leading to, for instance, fewer LKFs with long lifetimes (Hutter & Losch, 2020). In contrast, the model output fields provide deformation data for the whole study region without any gaps in time. Thus, we mask the LKFs detected in each simulation with the RGPS coverage in order to exclude any effects of varying RGPS coverage on the comparison between model and observations. The tracking of LKFs is repeated only for the masked LKFs. We use the masked LKFs for all statistics presented in this paper, because these results are directly or indirectly affected by the number, length, or lifetime of the LKFs. The original unmasked LKFs are only used in the concentration and thickness anomaly analysis, as we do not compare to RGPS data in this analysis, and in the intersection angle analysis, because in the coarse resolution simulations there are otherwise too few LKFs available for this analysis. We tested with all high-resolution simulations that masking the LKFs with the RGPS coverage does not affect the distribution of simulated LKF intersection angles (not shown).

A direct comparison of LKFs detected in RGPS and model output is not possible due to the chaotic nature of ice fracture (Coon et al., 2007; Kwok et al., 2008). Instead, statistics of the spatial and temporal properties of the simulated features can be compared to the statistics derived from observations (Hutter & Losch, 2020). This paper focuses on a comparison between the probability distribution functions (PDFs) of LKF properties related to space (length, intersection angle) and time (lifetime, growth rates). In addition we study the density of LKFs described by the regional distribution of relative LKF frequency. To properly evaluate the simulations with RGPS, we seek a quantitative way to compare the PDF of a given LKF property obtained from model and RGPS LKF data. Most of these distributions have a heavy tail so that standard metrics, such as the Kolmogorow-Smirnov statistic or the Wasserstein distance, cannot be applied. Instead we define the skill metric as the integral of the difference between two (more specifically, between RGPS and simulation) PDFs of a given property on a logarithmic scale. We choose this metric as it is closest to the visual comparison of the PDFs and it emphasizes the tail of the distributions. For clarity and consistency, we also use the same statistic to define the misfit in intersection angles, although the data is not heavy tailed. By using the log-scale in the skill metric all parts of the intersection angle PDFs are weighted without overemphasizing the peak of the distribution. As not all simulations contributing to SIREx are run over the same time period, we use the RGPS years consistent with each simulation in the computation of the metric functional. In this manner, we take interannual variability of the LKF statistics between both SIREx winters into account. By definition the skill metric increases with larger misfit between model and observations. Thus, a lower skill metric value indicates better model performance.

For reference of the magnitude of the skill metric, we use the interannual variability of different LKF properties within the RGPS data set. To this end, we compute the PDFs of each property for all RGPS winters (JFM 1998 to 2007) individually. Comparing these PDFs with both SIREx winters, reference values are computed using the same "skill" metric as for comparison between the simulations and RGPS data. For each property, we average the computed "skill" values of all years to quantify the interannual variability that can be compared to the computed models' skill. We note here that for quantities with little year-to-year variability, for example, the intersection angle, the interannual variability is a reasonable benchmark to assess model performance. For quantities that are thought to be affected more strongly by wind patterns and ice condition and thus vary stronger from year to year (e.g. LKF density), the interannual variability provides a maximum of the skill metric that should not be exceeded by a model simulation to be called useful.

4 Simulated deformation features

In this section, we present the characteristics of the simulated LKFs and compare them to satellite observations. First, we describe the overall number of LKFs in each simulation and their regional distribution, followed by an analysis of the spatial properties, length and intersection angle, and the characteristics related to time, lifetime and growth rate. We include a short metric-specific discussion of the results in this section. The relation between specific model parameters on the skill values of simulated LKFs is discussed specifically in Section 5.

4.1 Number of simulated LKFs

Recent sea-ice modeling studies described in a qualitative way how the number of resolved deformation features varies with model parameters (e.g., Bouillon & Rampal, 2015; Q. Wang et al., 2016; Spreen et al., 2016), but only very few quantified these variations (Koldunov et al., 2019; Hutter & Losch, 2020). Visual analysis of deformation fields does not provide enough information to distinguish the tendencies in the number of LKFs and the total length of all LKFs, as both are proportional to the total number of grid cells associated with LKFs. Our object-based approach allows assessing both properties in a quantitative way. In Fig. 1(a) we present how the numbers of detected LKFs changes with model resolution for the SIREx simulations. Fig. 1(b) shows the total length of all LKFs as function of the model resolution. For the discussion, the total length of all LKFs is more interesting, because it is directly related to the total area of potential air-ice-ocean interactions, whereas the number of LKFs does not include the length, and hence, area information.

For our set of simulations we find that both the number of LKFs (Fig. 1a) and the total length of all LKFs (Fig. 1b) increase as the grid resolution becomes finer, even though for both metrics there is considerable variation also between simulations with the same grid resolution. Note that we can not comment on the effect of the resolution for EAP and MEB, as there are only simulations using these rheologies in our comparison at one specific resolution. Most models underestimate both the number of LKFs and their total length. MITgcm (2km, ITD) agrees with RGPS data in the total length of all LKFs, but has too many LKFs indicating that too short LKFs are simulated (see the PDFs of LKF length in Fig. 4).

Besides the effect of grid resolution, some other model parameters seem to affect the number of LKFs as well: (1) More ITD classes lead to more resolved LKFs in the simulations, and to an increase of the total length of all LKFs as seen by comparing MITgcm (2km) and FESOM2 to MITgcm (2km, ITD), or by comparing ANHA (4km), FESOM, and MITgcm (4.5km) to HYCOM-CICE (FSU) and RIOPS. All simulations listed here use an (E)VP rheology. (2) The comparison of RASM-WRF (both EAP and EVP simulations) with RASM-CORE2 (EAP) suggests that coupling the sea-ice model to an interactive atmosphere rather than forcing it with atmospheric reanalysis increases the number of resolved LKFs. While this is plausible, because prescribed forcing generally suppresses internal variability, the available simulations alone do not allow to conclude

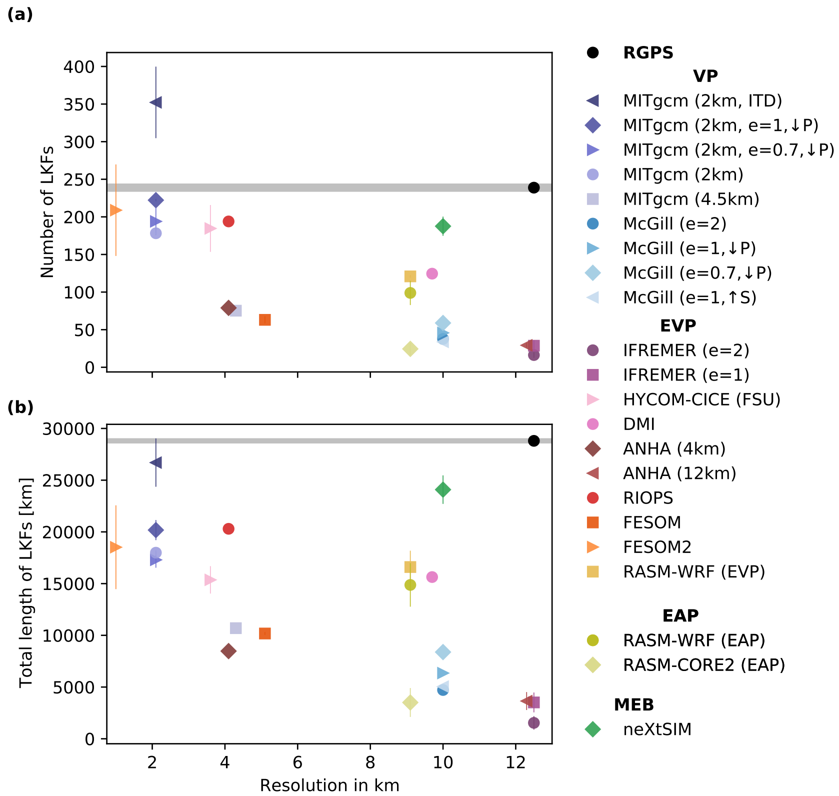

Figure 1. The average number of detected LKFs in three day intervals (a) and the total length of all LKFs together in three day intervals (b) in all simulations as a function of spatial grid resolution. The inter-annual variability of LKF number and length for each model that contributed simulations for two years is shown as a thin vertical line around the multi-year mean. The thin gray lines represent the RGPS value across all spatial resolution for reference.

if the increase in LKFs is caused by the coupling itself or the higher spatial and temporal resolution of the wind fields driving the ice. We note here that the coupled RASM simulation also use an increased number of EVP subcycles, which also likely improves the LKF representation. A coupling time step of 20 min as in RASM-WRF allows to resolve inertial oscillations leading to higher variable wind forcing that potentially initiates the formation of additional LKFs. Simulations using very high spatial and temporal resolution atmospheric forcing also tend to show better agreement with observations than simulations forced by medium resolution winds (ANHA (4km), FESOM, and MITgcm (4.5km) vs. HYCOM-CICE (FSU) and RIOPS; DMI vs. McGill). (3) The neXtSIM simulation shows results much closer to observations than other simulations with similar resolution. Its grid resolution of 10 km is in the range of all models, still this simulation stands out for the potential following reasons: It is the only simulations to use a brittle rheology (MEB) and it uses a Lagrangian modeling approach (i.e. an unstructured moving grid) and high resolution atmospheric forcing. This makes it difficult to clearly separate the effects of the individual parameters. The similarity of the two FESOM simulations, which also use unstructured, but fixed grids, with the MITgcm simulations of similar resolution suggests that the type of grid itself has little effect. The relatively high resolution forcing (40km or less) will add more variability to the system, but does not guarantee good agreement with RGPS observations (see e.g., RIOPS HYCOM-CICE (FSU), DMI), so that the MEB rheology — potentially when associated with a Lagrangian grid — appears to be responsible for the better agreement with observations. Clearly, a direct comparison of MEB and VP rheologies in the same model framework (grid, forcing, etc.) is required to illustrate the differences between these different rheology approaches.

4.2 Regional distribution

There are LKFs in the entire Arctic Ocean, but particularly high densities are found along coastlines and bathymetric features (shoals and continental slopes), with sightly pronounced densities in the Beaufort sea, and low densities in fast ice regions (Mahoney et al., 2012; Wernecke & Kaleschke, 2015; Willmes & Heinemann, 2016; Hutter et al., 2019). The distribution of LKFs in the SIREx simulations have stronger regional variations than RGPS (Fig. 2). In general, there is a large spread in modeled LKF densities and their difference to the observed LKF densities (Fig. 3). Indeed, nearly all models strongly underestimate LKF densities by far more than the range of interannual variability of RGPS. As expected from the analysis of the number of LKFs, low resolution models using (E)VP or EAP rheologies tend to underestimate the LKF density more than high resolution models. The largest differences are mainly in the pack ice area (here defined as sea ice regions that are more than 150 km away from the coastline) with generally too few LKFs compared to observations. In coastal regions the distribution of LKFs is better reproduced with half of the models showing differences within the range of the RGPS interannual variability. Along the closed boundary of the coastline stress concentrates and initiates ice fracture. Our results indicate that this process forms LKFs independent of the model's grid resolution.

In the pack ice area, only the MITgcm (2km, ITD) and the neXtSIM simulation produce overall LKF densities within the interannual variability of RGPS (both in pack ice and the entire Arctic). Both models use mechanisms to locally reduce the ice strength based on the deformation history, which initiates fracture in pack ice (the direct deformation feedback by damage parameterization in neXtSIM and the indirect deformation feedback on the ice strength defined in Rothrock (1975) by preferred opening in lower ITD classes). We analyzed only two model winters, but the interannual variability of LKF distribution in the RGPS data set is small, so that the underestimation of sea ice deformation in the pack ice area by nearly all models is very likely a general issue in every year.

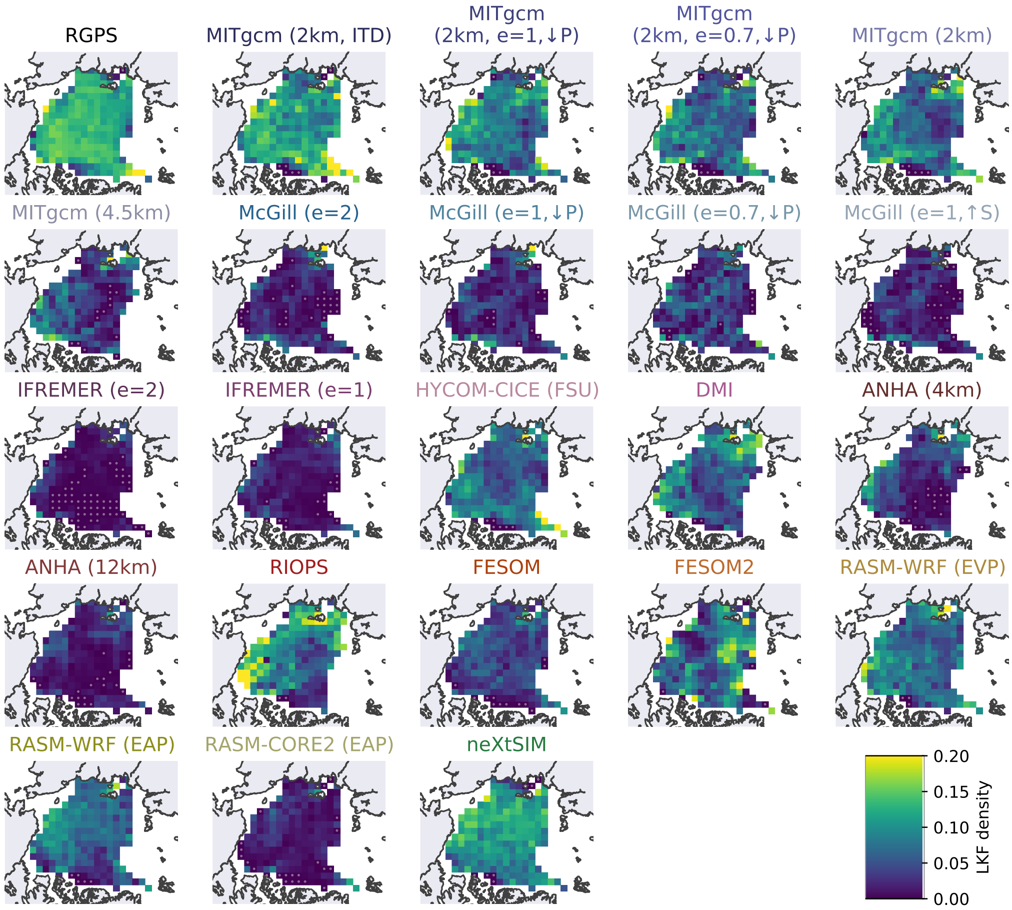

Figure 2. LKF densities for RGPS and all models defined as the relative frequency of LKFs within 150×150km boxes in a Polar stereographic projection normalized by the number of deformation observations available for the box. Cells without any LKF are indicated by a grey dot. Note that the RGPS coverage for both SIREx years is different leading to a slightly different masks for the simulations.

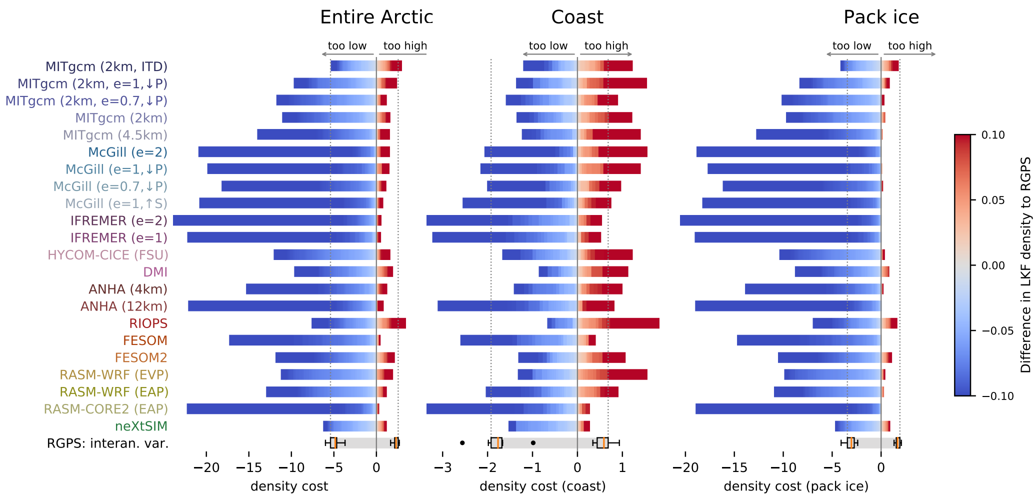

Figure 3. Cumulative box-wise differences of LKF density for all simulations compared to RGPS separated into three regions: entire Arctic (left), within 150 km of the coastline (middle), and pack ice area 150 km away from the coastline (right). Regions where models underestimate LKF densities are accumulated in the blue bar, while the overestimation of LKF densities is given by the red bar. The two colormaps indicate the size of the over- or underestimation in each grid cell. In the bottom row, we illustrate how the RGPS LKF densities of the other RGPS years differ from the two SIREx winters. Two boxplots show this interannual variability of both under- and overestimation. The dotted grey lines show the first quartile of the underestimation and the third quartile of the overestimation of LKF densities in all RGPS years as a reference range for LKF densities.

4.3 LKF length

Deformation features criss-cross the sea ice cover at ranges from meters to multiple kilometers (Kwok, 2001). The distribution of LKF lengths in the RGPS data set is heavy-tailed and can be described by a stretched exponential distribution (Hutter et al., 2019), which is consistent with the notion of scale-invariant sea-ice deformation. The LKF length distributions of all SIREx models also have fat tails (Fig. 4), even though most models overestimate the number of very long LKFs. This phenomenon is most pronounced for models with fewer LKFs (see 4.1). Some models (FESOM2, HYCOM-CICE (FSU), MITgcm (2km, ITD), MITgcm (2km, e=1,↓P), MITgcm (2km, e=0.7,↓P)) overestimate the amount of small LKFs thereby overly steepening the tail of the distribution. An obvious reason for this it that if more LKFs cover the same area it is more likely that the intersection with other LKFs makes them shorter (Hutter & Losch, 2020). Only HYCOM-CICE (FSU) and both MITgcm (2km, ↓e) simulations with reduced ellipse ratio reproduce the LKF length distribution within the range of the reference, which represents the interannual variability of the RGPS data set.

4.4 Intersection angle

The material properties of sea ice affect the intersection angle of its deformation features (Erlingsson, 1988; K. Wang, 2007), and intersection angles have been used to evaluate the dynamics of high resolution sea-ice simulations (Heorton et al., 2018; Ringeisen et al., 2019; Hutter & Losch, 2020). Acute intersection angles ranging around 30°–50° have been reported from both satellite imagery (Walter & Overland, 1993; Cunningham et al., 1994; E. M. Schulson & Hibler, 2004; K. Wang, 2007) and laboratory measurements (E. Schulson et al., 2006). These studies focused on intersecting LKFs, so-called conjugate faults, that form simultaneously under the same compressive forcing. The distribution of intersection angles in the RGPS LKF data set also peaks in this range (see Fig. 5 and Hutter et al., 2019). For an intersecting pair of LKFs, two intersection angles can be computed, both of which add up to 180°. For conjugate faults the fracture angle of each LKF δ is measured relative to the direction of compressive stress with the intersection angle summing up to 2δ. Except for laboratory experiments, the direction of stress is unknown, also in the SIREx simulations and RGPS. The stress states causing the deformation, however, can be also deduced from the resulting sea ice drift (see Appendix B). In this study, we introduce a new approach using the vorticity of two intersecting LKFs to interpret the deformation behavior at the intersection. The vorticities of two LKFs of a conjugate fault are of different sign, such that we can determine a main direction of compressive stress and choose an intersection angle (0° to 180°) relative to this direction. Using this method, we determine that roughly one third of intersecting pairs of LKFs in RGPS are conjugate faults. If the vorticities of both LKFs have the same sign, there is no clear stress direction. In this case, both potential intersection angles are taken into account when computing the distribution of intersection angles but weighted down by a factor of two. The distribution of intersection angles is computed for all SIREx models (Fig. 5). We do not mask the LKFs with the RGPS coverage, because some models with very few LKFs do not show intersecting LKFs within the region covered by RGPS. For all other models with intersecting LKFs within the RGPS coverage, we have tested that the region of the analysis does not affect the distribution of intersection angles significantly (not shown).

We find that the distributions of intersection angles in all models peak around 90°, in strong contrast with the peak at 45° for RGPS observations. Only for the McGill simulations with non standard yield curves (e=1,↑S; e=0.7, ↓P; e=1, ↓P; these values of e are outside the commonly used range, but they still follow the principle that ice is stronger in compression than in shear), there is a peak around 55°. However, these simulations also produce a second peak of similar magnitude at $180° - 55° = 125°$. This peak can mean that (1) the corresponding intersecting pairs are not formed under uniaxial com-

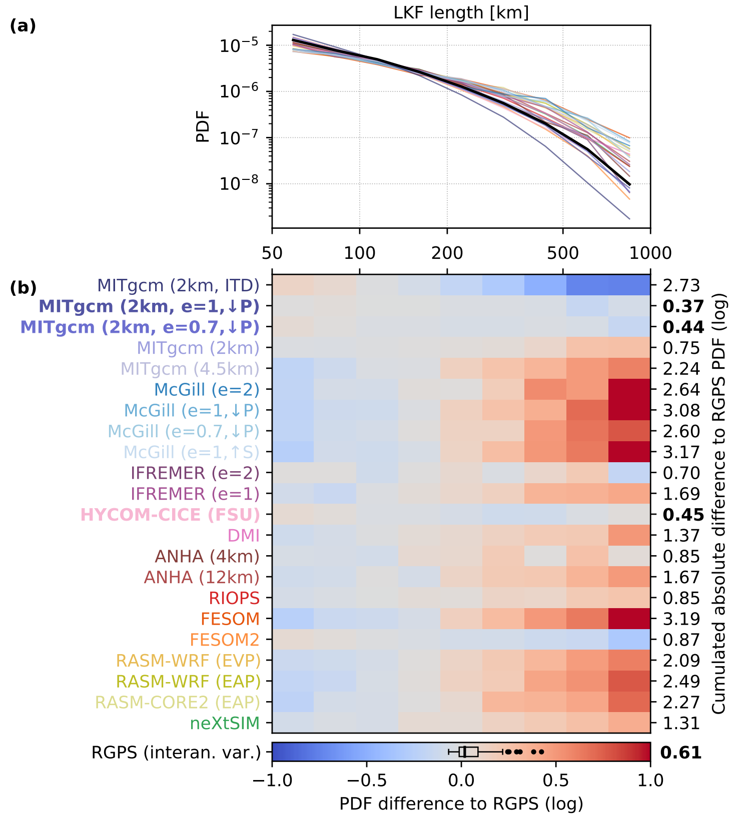

Figure 4. (a) Distribution (PDF) of LKF lengths for all models and RGPS. The color references for the models are provided in (b). The difference between the PDFs of simulated LKF lengths and RGPS LKF lengths is shown in (b) for each model. A scalar metric for LKF length is the integrated area between the LKF length PDF of the model and RGPS, given on the right hand side. As reference we compute the differences between the LKF length PDFs of all RGPS years and the two SIREx years to quantify the interannual variability. The differences in all bins and all RGPS years are summarized in the box plot given in the colorbar. The reference value of this metric for the interannual variability is computed and provided at the right hand side of the colorbar.

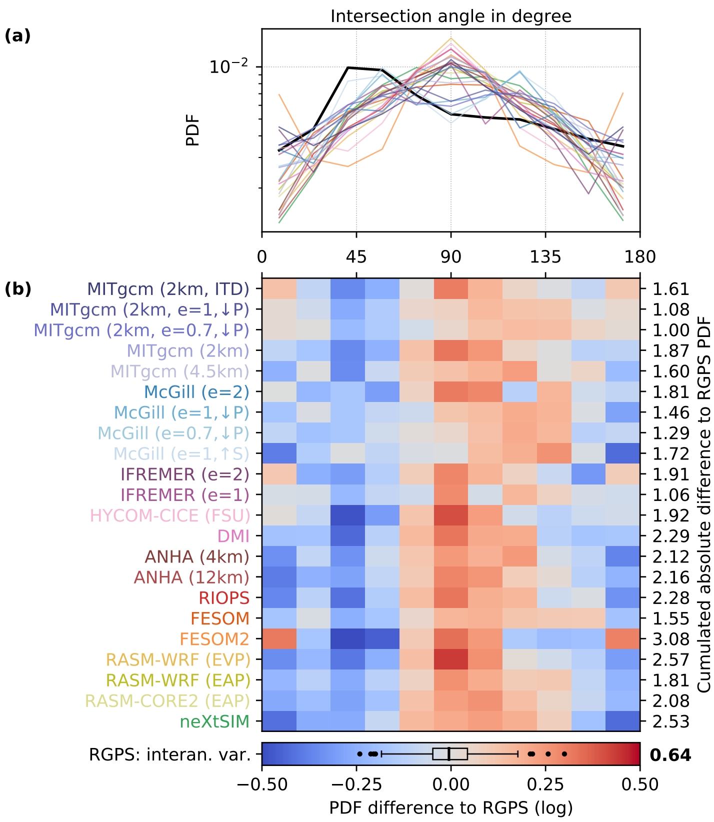

Figure 5. (a) Distributions (PDF) of intersection angles between pairs of LKFs for RGPS and all models. The color references for the models are provided in (b). The difference between the PDFs of simulated intersection angles and intersection angles observed with RGPS is shown in (b) for each model. A scalar metric for intersection angles is defined as the integrated area between the intersection angle PDF of the model and RGPS. For each model the value of this metric is given at the right hand side of (b). The interannual variability in the RGPS data set is presented in the same way as in Fig. 4. Note, that the intersection angles are not periodic data as we define them relative to the stress direction.

pressive forcing, or (2) the yield curve settings allow a wider range of intersection angles. The normal flow rule used in these models determines the fracture angle to be normal to yield curve at the stress state of the fracture (Ringeisen et al., 2019). By decreasing the ellipse aspect ratio e, the fracture angle varies more strongly with the stress state assuming that shear deformation is dominant. This could cause the larger variety of intersection angles in these simulations. This interpretation is supported by the fact that the MITgcm and IFREMER simulations with reduces ellipse ratio (e=0.7 and e=1) simulation leads to a broader distribution of intersection angles compared to the simulations with the standard ellipse ratio (e=2).

The three simulations with rheologies for which the previous reasoning does not apply (neXtSIM, RASM-CORE2 (EAP), and RASM-WRF (EAP)) also produce a peak at 90°, while compared to (E)VP simulations the peak is broader showing similar probabilities for intersection angles between $70°-110°$. The strong underestimation of small intersection angles compared to RGPS, especially in the neXtSIM simulations, results in a larger overall misfit between simulated and observed PDF distributions than for VP/EVP simulations.

Experiments with simple geometry and uniform forcing suggest a clear connection between rheology and intersection angles (e.g. Ringeisen et al., 2019, 2020). The SIREx simulations with realistic forcing and realistic geometry produce a large variety of stress states that eventually lead to deformation. This is manifested in the broad distributions of intersection angles (Fig. 5). Some models that use atmospheric forcing with low resolution have a better representation of the intersection angles compared to observations. We speculate that the stronger gradients in high resolution atmospheric forcing partly imprint on the simulated deformation field, which reduces the impact of the rheology on simulated intersection angles and explains why all rheologies lead to similar angle distributions. However, observations point towards a distinct peak of intersection angles that depends less on the forcing conditions. Thus, the apparent connection between wind forcing and simulated intersection angles in the simulations in this study does not appear realistic and points to problems in the model physics.

4.5 LKF lifetimes

The lifetime of an LKF describes the period when the LKF actively deforms. The lifetime of LKFs together with the area covered by LKFs are key factors for air-ice-ocean interaction. For instance, the overall heat loss through a lead strongly depends on its opening time. The majority of LKFs are active for less than 3 days, but the distribution of LKF lifetimes shows an exponential tail such that LKFs up to a month old can be observed as well (Kwok, 2001; Hutter et al., 2019). For both SIREx years, RGPS recorded on average shorter LKF lifetimes compared to the other RGPS years. This is likely to be caused by exceptional wind forcing leading to enhanced LKF formation and rapidly varying satellite coverage that makes tracking of LKFs more difficult. Here, both effects reduce the LKF lifetimes. As we use atmospheric reanalysis to drive the simulations and mask the simulated LKFs with the satellite coverage for this analysis, all models are expected to reproduce these shorter lifetimes.

All SIREx models agree with RGPS in the sense that LKFs younger than 3 days are most abundant. In addition, the lifetime distributions of simulated LKFs follow an exponential tail for all SIREx models (Fig. 6). The only exception is ANHA (4km) with no LKFs older than 15 days. In both IFREMER simulations there are no LKFs lifetimes longer than 21 days.

Most models overestimate the relative frequency of long-lived LKFs and produce a too slow decay rate of the exponential tail. This is particularly the case for simulations with low absolute LKF numbers, for which LKFs concentrate in coastal regions. Coastal LKFs, like flaw leads, are a frequently occurring and stable phenomena, as they are mainly

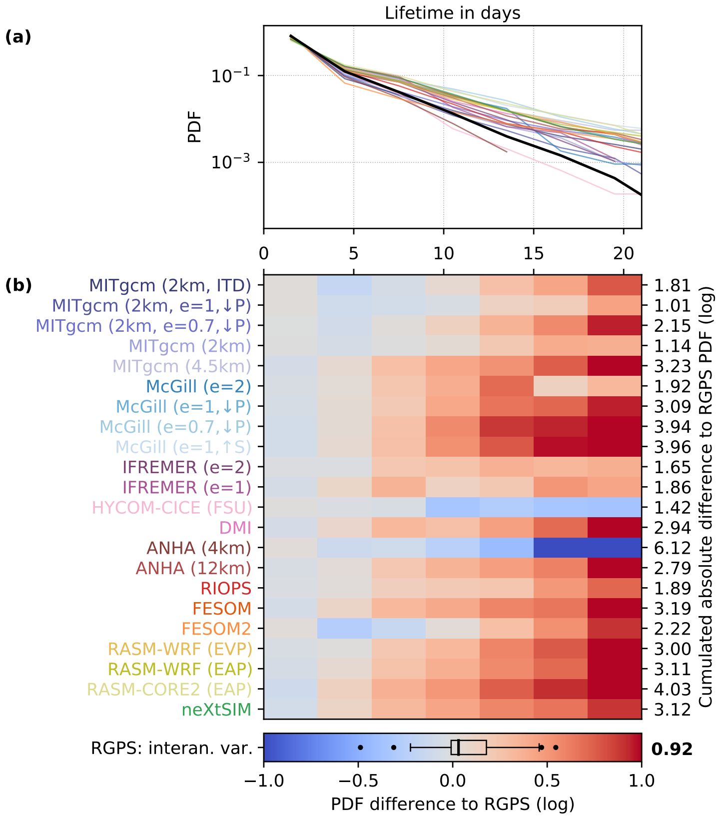

Figure 6. (a) Distribution (PDF) of LKF lifetimes for RGPS and all models. The color references for the models are provided in (b). The differences between the PDFs of simulated lifetimes and lifetimes observed with RGPS are shown in (b) for each models. The scalar metric for lifetime is defined as the integrated area between the lifetime PDF of each model to RGPS normalized by the interannual variablilty in the RGPS data set. For each model this value is given at the right hand side of (b). The interannual variability in the RGPS data set is presented in the same way as in Fig. 4.

determined by coastal geometry. Thus, LKF lifetimes are likely to be overestimated in simulations that show too many coastal LKFs compared to LKFs in the pack ice area. Simulations with a better representation of LKFs in the pack ice area also reduce the overestimation of LKF lifetimes (e.g. FESOM2, RIOPS, HYCOM-CICE (FSU), MITgcm (2km), MITgcm (2km, e=1,↓P)). We speculate that this remaining overestimation may have its root in the deformation ice-strength feedback initiating LKF growth in non brittle models: the strong deformation localized in LKFs leads to a reduction in concentration and thickness, which reduces the ice strength. In the next time step, the reduced ice strength makes deformation in the same grid cell more likely. The locally incurred thickness and concentration anomalies can only be reduced by converging ice motion or thermodynamic ice growth. The overestimation of LKF lifetimes by VP, EVP, and EAP models indicates that the memory of past deformation associated with this feedback may be too strong. Instead of this deformation ice-strength feedback, the MEB rheology of the neXtSIM model uses a sub-grid-scale damage parameterization that scales the ice strength based on how strongly the stress exceeds the Mohr-Coulomb yield criterion. The memory of the damage parameter is limited by a healing time parameter that is independent of the thermodynamic parameters. Although neXtSIM overestimates the LKF lifetimes as other models in our comparison, neXtSIM simulations with a modified damage criterion (not shown) have shown better agreement with RGPS LKF lifetimes. Thus, tuning the healing parameter could probably improve the overestimation of LKF lifetimes in neXtSIM.

4.6 LKF growth rates

In this section we study how quickly LKFs grow and shrink. We define the LKF growth rate as the change in length of an LKF between two records (for definition see Hutter & Losch, 2020). In our analysis, we combine three different growth rates: the initial growth of the LKF at formation, and the growing and shrinking of persistent LKFs. We find that the distribution of growth rates shows a heavy tail for RGPS data and all models (Fig. 7). The majority of the models overestimate large growth events. We note that most of these models also produce too few LKFs (Sec. 4.1). Models that overestimate the number of LKFs (neXtSIM and MITgcm (2km, ITD)) show fewer large growth rate events. We find a similar dependence on the number of LKFs for the distribution of LKF lengths and note here that the models' performance in terms of LKF length and growth rates are correlated. This correlation emerges because the temporal resolution of 3 days is not high enough to accurately observe the speed with which a fracture in the ice can propagate through the entire Arctic Ocean. Propagation speeds in the sea ice cover are linked to elastic wave speeds and range from 10 to 1000 m/s (Stamoulis & Dyer, 2000; Marsan et al., 2011; Dempsey et al., 2012). Thus, the growth rates computed for our 3-daily data are limited by the length of the LKFs. Still, all reported growth rates are within a physically reasonable range. In particular, the fact that we find very high growth rates in all simulations shows that all rheological frameworks in our comparison simulate fast fracture propagation. A temporal sampling rate of seconds to minutes would be required to avoid the limiting effect of LKF length and determine the actual fracture speed of the models.

4.7 Summary of LKF properties

Values of all LKF statistics and all simulations are summarized in Fig. 8, where all skill metrics are normalized with the RGPS interannual variability. A cumulative skill metric is computed from the weighted average of all model metrics. In this weighted average, both density metrics (distribution and total length) are considered and the lifetime metric is weighted by a factor two in order to take into account that these skill metrics are most relevant to interaction processes along LKFs in coupled climate simulations. We find that no model in the comparison is able to reproduce the spatial and tempo-

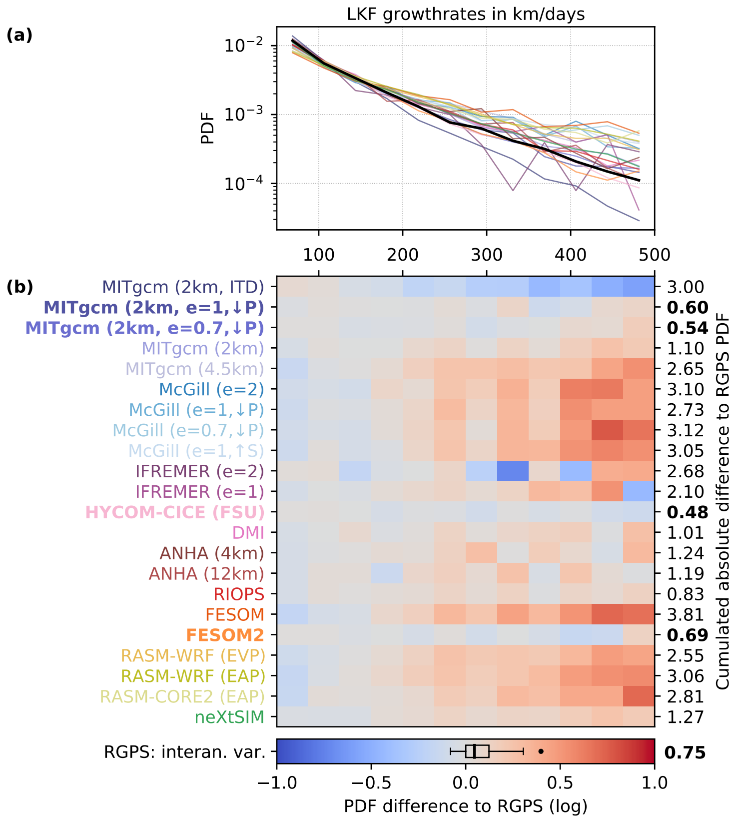

Figure 7. (a) Distribution (PDF) of LKF growth rates for RGPS and all models. The color references for the models are provided in (b). The differences between the PDFs of simulated growth rates and growth rates observed with RGPS are shown in (b) for each models. The scalar metric for growth rates is defined as the integrated area between the lifetime PDF of each model to RGPS. For each model this value is given at the right hand side of (b). The interannual variability in the RGPS data set is presented in the same way as in Fig. 4.

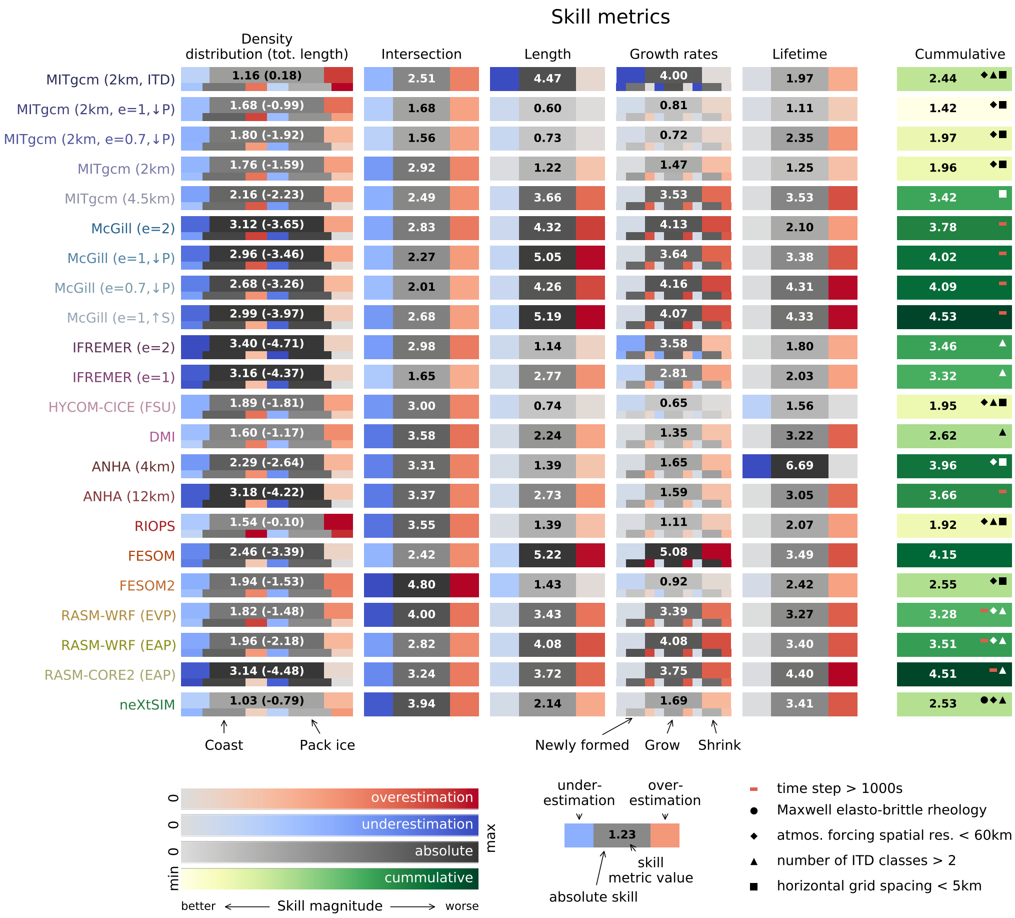

Figure 8. Summary table of the individual model skill metrics. Each entry provides the absolute value of the metric as a number along with a grey color code. All model values are normalized with the interannual variability for the given property in the RGPS data set, that is, model values within the RGPS interannual variability are smaller than one. The magnitude of the underestimation and overestimation contributing to the skill metric value are shown in blue and red color code. For density two skill metric values are computed: the sum of over- and underestimation as a measure for the entire distribution of LKFs and the difference between both as a measure for the overall area covered by LKFs. The last column provides the weighted sum of all skill metrics for each model. To put more emphasis on properties that are mostly relevant to air-ice-ocean interaction processes along LKFs, we take both densities metrics (distribution and total length) into account and scale the lifetime metric by a factor of 2. Details of the model configuration that help to explain the overall performance of individual models are provided by footnotes to the cumulative skill metric.

ral statistics of LKFs within the range of the interannual variability of the RGPS data set, as all simulations have cumulative skill metrics larger than 1. The best simulations in the comparison (MITgcm (2km, e=1, ↓P), MITgcm (2km, e=0.7, ↓P), MITgcm (2km), HYCOM CICE (FSU), RIOPS) show cumulative skill metric values between 1 and 2. The cumulative skill metric values of MITgcm (2km, ITD), DMI, FESOM2, and neXtSIM range between 2 and 3 showing an overall good performance but too high values for specific LKF statistics. The cumulative skill metric values larger than 3 of MITgcm (4.5km), McGill, IFREMER, ANHA, FESOM, and RASM are caused by large skill metric values for multiple LKF statistics. A common feature within these simulations is that they strongly underestimate the number of LKFs in the pack ice area, which negatively affects other statistics.

The good performance of some simulations is related to a combination of several aspects: high resolution atmospheric forcing, a high number of ITD classes, high spatial resolution, or a brittle rheology. In contrast, simulations with a large time step have higher cumulative skill metric values. In Section 5 we will discuss these dependencies in more detail.

In the summary table of all model skill metrics (Fig. 8) links between different LKF statistics become apparent: (1) An overestimation of LKF density coincides with too short LKFs (MITgcm (2km, ITD)) and vice versa (McGill, FESOM, and RASM). (2) Simulations that overestimate LKF lengths likely overestimate LKF lifetime as well. (3) The skill metrics for LKF length and LKF growth rates are correlated, because the low temporal resolution of the data does not allow to study the actual propagation speed of ice fracture.

5 Relationship between model configuration parameters and deformation features

In this section, we study how different parameters of the model configuration affect the LKF statistics to provide advice for the configuration of sea-ice models. The following configuration parameters are considered: grid spacing, time step, number of ITD classes, spatial and temporal resolution of the atmospheric forcing, and rheology. The dependence of the model performance on the choice of the parameters is investigated by employing a linear regression (Fig. 9). The wide spread of skill metric values for similar configuration parameters illustrates the high sensitivity of sea-ice models to parameter combinations and different code implementation of model physics. Despite the large spread, some trends emerge and provide guidance on how to appropriately choose model parameters. We need to be cautious with making inferences from the intersection angle metric, as all simulations produce too large intersection angles. Some models with a slightly better skill in intersection angles use somewhat extreme parameters (e.g. 3600s time step, very coarse resolution atmospheric forcing). The implications may be misleading, also because these models usually have poor skill scores in other LKF statistics such as density and lifetime. We note that, rather than tuning configuration parameters studied in this paper, model physics need to be adapted to improve the intersection angles skill.

From all configuration parameters, the time step of the simulation and the spatial resolution of the atmospheric forcing have the strongest effect on the skill metrics, mainly their density, length, and growth rates ($r^2 > 0.25$). Increasing the spatial resolution of the model only improves the density of deformation feature. Thus, the effect of a small time step on LKF length and growth rate is independent of the coupling between high resolution and short time step. LKF lifetimes are not significantly affected by the choice of any of considered configuration parameters. A high temporal resolution of the atmospheric forcing improves the simulated LKF length distribution and LKF growth rates ($r^2 \approx 0.2$). Horizontal grid spacing (Spreen et al., 2016; Hutter et al., 2018), rheology

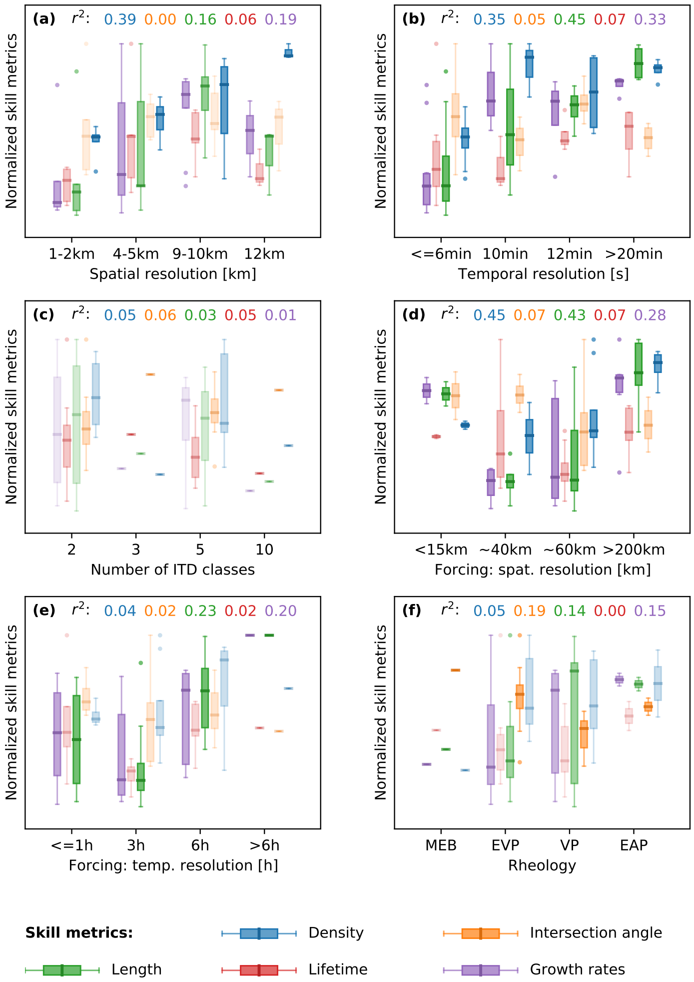

Figure 9. Box plots showing the dependence of the individual skill metrics on the following configuration parameters used in the simulations: (a) spatial resolution of the model, (b) temporal resolution, (c) number of ITD classes, (d) spatial resolution of the atmospheric forcing, (e) temporal resolution of the atmospheric forcing and (f) rheology. The skill metric values on the y-axis are normalized. For each combination of skill metric and model parameter a linear regression analysis is performed and the r^2-value of all regressions is summarized at the top of each subfigure. The box plots are faded with decreasing r^2-value, where saturated colors represents skill model-parameter combinations with $r^2 > 0.25$.

and ice strength parameters (Hutchings et al., 2005; Girard et al., 2011; Rampal et al., 2016; Bouchat & Tremblay, 2017), and solver accuracy (Q. Wang et al., 2016; Koldunov et al., 2019) have been reported to have an effect on the amount of LKFs in Pan-Arctic simulations, while so far time stepping and atmospheric forcing have not been studied in realistic model configurations. In idealized sea ice model configurations, improvements in the scaling characteristics of sea ice deformation were found for experiments driven by high-resolution atmospheric forcing fields (Hutter, 2015) in agreement with the findings presented here.

More simulations using an MEB or EAP type of rheology are needed to robustly disentangle the effect of the rheology on LKF simulations from the effect of other parameters. Both rheologies are only used by one model each. All RASM configurations show very high cumulative skill metric values, also for the EAP simulations. Comparison of the RASM simulations using the EAP rheology versus RASM-WRF (EVP) shows that LKF intersection angles are better reproduced, however the skill of the simulation with the EAP rheology in terms of the other LKF properties is lower than that in the RASM-WRF. The neXtSIM simulation with the MEB rheology generally reproduces LKFs statistics in closer agreement with RGPS than the (E)VP simulations at the same resolution. The neXtSIM model is also the only model running on a Lagrangian grid, which therefore does not allow us to undoubtedly conclude from this study on the respective importance of the rheology versus the advection scheme. In addition, the neXtSIM simulation are driven with relatively high resolution atmospheric forcing ($\sim$40 km), which may have a positive effect on the LKF skill metrics. The combination of its brittle rheology and the use of a Lagrangian moving mesh allows neXtSIM to achieve a good representation of LKFs despite the coarser grid spacing — as it was designed to do.

Three (E)VP models (MITgcm, McGill, and IFREMER) in the comparison run sets of simulations that differ only in yield curve parameters, namely the compressive ice strength parameter P^* and ellipse ratio e. In these simulations, the yield curve parameters have an impact on the LKF quality. For all models we find that simulations with reduced ellipse ratio show improved LKF densities compared to the simulations with standard ellipse ratio $e = 2$, as one could expect from the more localized deformation in these simulations (Bouchat & Tremblay, 2017; Bouchat et al., 2020). For other LKF statistics the effects vary from model to model and might therefore dependent on other configuration parameters that are different between the models, for instance resolution. We note, however, that three of the five models with the lowest cumulative skill metric value (< 2) in our comparison use an reduced ellipse ratio (MITgcm (2km, e=1, ↓P), MITgcm (2km, e=0.7, ↓P), RIOPS (e=1.5)). In contrast to the ice strength, the ellipse ratio has rarely been considered as tuning parameter in systematic parameter optimizations of sea-ice models. Nevertheless, the few studies that include the ellipse ratio in their optimization to our knowledge (Ungermann et al., 2017; Sumata et al., 2019) show that a reduced ellipse ratio also improves the simulated sea-ice extent, volume, and drift. Therefore, we recommend to also adjust the ellipse ratio to reduce the overall model-observation misfit.

6 Relationship between LKF statistics and scaling analysis of deformation

Scaling analysis of sea-ice deformation has been the main tool to evaluate the realism of lead-permitting sea-ice simulations. There are indications, however, that the computed scaling exponents are linked to the number of LKFs, but do not provide insights in other LKF statistics such as LKF lifetime or intersection angles (Hutter & Losch, 2020). In this section, we study if the deformation statistics obtained in SIREx part I (Bouchat et al., 2020) are linked to the LKF statistics in this study. To this end, we define skill metrics for the deformation rate PDFs (as the sum of the integrated area between the divergence and shear PDF of a SIREx simulation and RGPS) and for all scaling param-

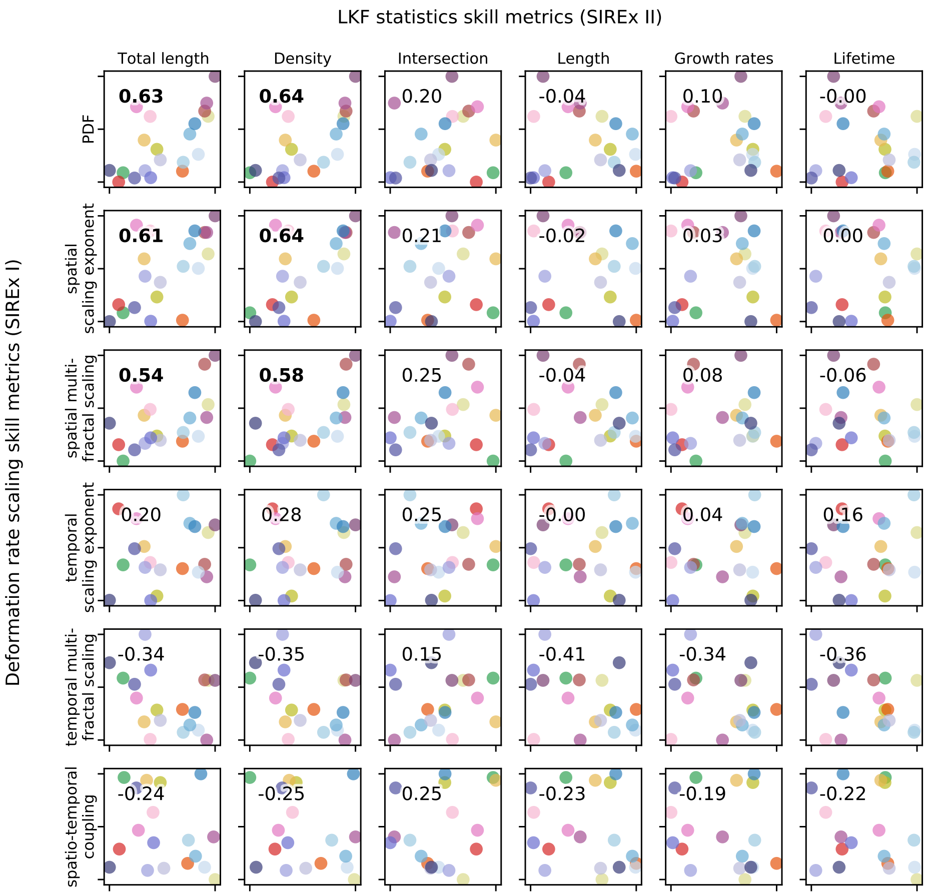

Figure 10. Relationship between skill metrics of the scaling analysis of deformation rates (SIREx Part II, Bouchat et al., 2020) and the skill metrics of the LKF statistics. For each combination of skill metrics a scatter plot is shown, where the correlation coefficient between both skill metrics is given in upper right in each subplot.

eters (relative error of the parameter compared to RGPS, e.g. $(\beta_{model} - \beta_{RGPS})/\beta_{RGPS}$). In this analysis, we group and average the multi-fractal parameters (degree of multi-fractality μ, fluctuation exponent H, and degree of heterogeneity C_1 – Bouchat et al., 2020) together to one skill metric each for spatial and temporal multi-fractal scaling. We test the correlation between all these deformation statistics metrics and all metrics defined for the LKF statistics (10). From all possible combinations, we only find a significant correlation ($> 50\%$) of the metrics for the PDF of deformation rates and LKF density and total length, as well as of the metrics for the spatial scaling exponent β and spatial multi-fractal scaling with the LKF density and total length (Fig. 10). All other combinations are not clearly correlated. This shows that good agreement of a simulation with observations in terms of the temporal (multi-fractal) scaling analysis or the more complicated spatio-temporal coupling of multi-fractal statistics does not guarantee realistic LKFs in the simulation. As the LKF density and total length are linked to the number of LKFs, our results generalize the findings of Hutter and Losch (2020) to a broader set of simulations. The link between the PDF of deformation rates and LKF density allows to use the PDF of deformation rates as an easy-to-compute metric to quickly assess a sea-ice simulation before using more sophisticated analysis like our feature-based comparison for a thorough evaluation.

7 Anomalies in sea-ice concentration and thickness along LKFs

So far we have defined LKFs as bands of deformation rates that exceed the local neighborhood. In the context of climate simulations, however, it makes sense to link LKFs to leads and pressure ridges, that is, reduced or increased sea-ice concentration or thickness, because the interaction of sea ice with the atmosphere and ocean strongly depends on the anomalies in the concentration and thickness fields. For instance, the sea-ice concentration and thickness in a lead determines the size of the heat fluxes from the ocean to the atmosphere. We compute estimates of concentration and thickness anomalies along LKFs for all SIREx simulations and visualize them in two dimensional PDFs (Fig. 11). We define the anomalies as the difference between the average concentration along an LKF and the local mean concentration, which is computed as the average around the LKF weighted by a Gaussian kernel of 150 km. We use the same definition for thickness anomalies. We determine the kernel size by balancing the two effects: (1) to be large enough to average out the LKF information itself, but (2) still be small enough to take into account regional variations in the sea ice concentration and thickness. The anomaly analysis is restricted to pack ice regions by taking only LKFs into account that are at least 150 km away from the coast.

The majority of LKFs shows little to no variation in the concentration and thickness field (on average +10.7 cm in pressure ridges and -12.8 cm in leads and +0.5 % in closing and -1.0 % in opening). Given the km-scale resolution of the models in this comparison, it makes sense that only some deformation features are associated with large-scale opening and closing, while the majority of LKFs represents smaller scale or pure shear deformation. The anomalies are caused by the divergent and convergent component of the deformation field along the line of failure of the ice that forms the LKF. The anomalies feed back into the ice strength favoring further deformation in sea-ice models using the standard Hibler (1979) ice strength. This positive feedback cycle of deformation - reduced concentration - further deformation can amplify the initial anomalies, make them persistent, and thereby lead to more LKFs. Obviously, the magnitude of the anomalies depends on the model grid resolution, as a much larger area needs to be opened or ridged in a coarse resolution model to obtain the same variation in sea ice concentration and thickness. Therefore the feedback cycle is enhanced with increasing resolution and the number of LKFs increases: The concentration anomalies in models with a resolution of ~ 5 km are as large as -10 %, while the simulations MITgcm (2km) and FESOM2 (1km) with even higher resolution feature LKFs with concentration reduction of

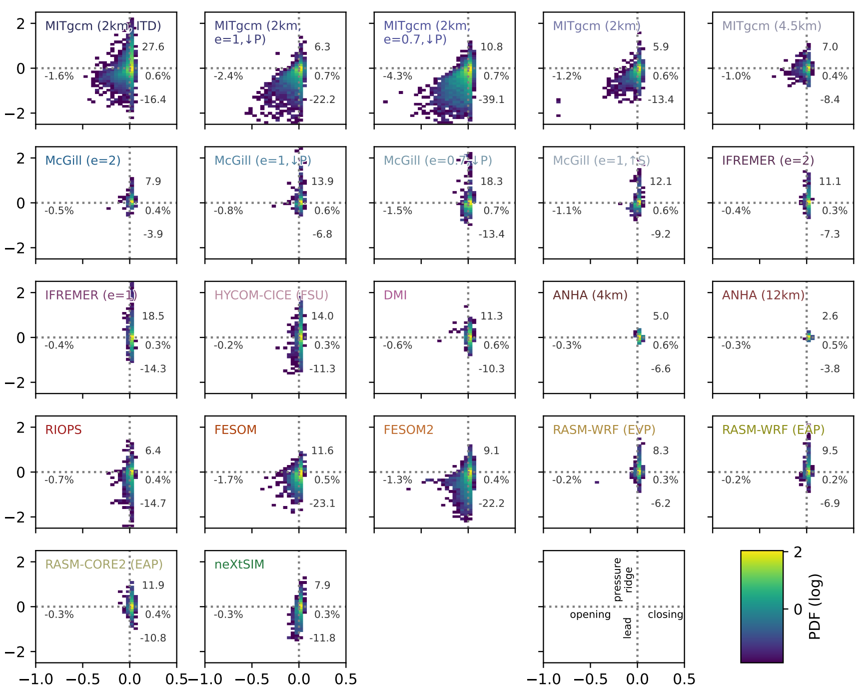

Figure 11. Concentration and thickness anomalies along LKFs for all models given in two dimensional PDFs. The anomaly is defined as the difference of average concentration and thickness along an LKF and the local mean of these fields that is determined by an average weighted by a Gaussian kernel of 150 km. Only LKFs in pack ice area are considered that are further than 150 km away from the coast. The numbers summarize the mean concentration anomalies for opening and closing, as well as the mean thickness anomalies for pressure ridges and leads given in centimeters. Note that, the interpolation of the model output of the simulations on unstructured grids (FESOM, FESOM2, and neXtSIM) to regular grids leads to a slight underestimation of the anomalies for these simulations.

the order of 50 % and higher. Also the average reduction over all openings in these simulations is higher than in the coarse resolution models.

In general, we find that thickness anomalies are more pronounced than concentration anomalies especially for coarse resolution models. In these models, the initial anomalies caused by deformation are smaller given the smaller effect of advection due to the large grid spacing. Therefore, the reduction in ice strength is less likely sufficient for further deformation and advection. Thermodynamic growth closes the ice cover, which slows down the deformation ice-strength feedback significantly and inhibits the deformation (the Hibler (1979) ice strength depends exponentially on the concentration and linearly on thickness). The thin ice in openings grows vertically only slowly by thermodynamic ice growth, so a long-term memory of deformation is retained in the ice. Under changed forcing conditions these long-term thickness anomalies are likely to be a seeding point for new deformation. To catch the effects of very short-lived concentration anomalies in climate simulations, short coupling time steps may be useful.

High-resolution simulations have the tendency to produce more negative thickness anomalies associated with leads than positive thickness anomalies that are found along pressure ridges, because the deformation ice-strength feedback accelerates opening. Only the MITgcm (2km, ITD) that uses an active ice thickness distribution together with the Rothrock (1975) ice strength stands out in this respect with a considerable amount of positive thickness anomalies with an average ridging of 27.6 cm. Simulations with reduced aspect ratio of the elliptical yield curve also produce higher mean ridging along LKFs (MITgcm, McGill and IFREMER), as with a "fat yield curve" convergent deformation is more likely for compressive stress states with confinement (Bouchat & Tremblay, 2017).

8 Conclusions

Linear kinematic features (LKFs) emerge in the sea-ice simulations with increasing resolution and/or with improved sea-ice physics. In this comparison between different sea-ice models and model configurations, only very few models reproduce some statistics of LKF properties, namely density, number, length, and growth rate, within an acceptable range as defined by the interannual variability of satellite-based RGPS deformation data. Most models, however, simulate unrealistic LKF distributions. This is particularly true for the intersection angle between pairs of LFKs, where none of the participation models reproduces the relative frequency distribution of observed angles. The LKF lifetime is also overestimated in nearly all simulations in the comparison. Even among the models with the highest skill scores, none simulates more than three LKF characteristics within the reference skill based on the interannual variability of satellite observations.

The models that have some skill use either high grid resolution, short time steps, different physics (brittle rheology or modified (E)VP yield curve), different numerical techniques (Lagrangian moving grid), high resolution atmospheric forcing in space and time, or a combination of these factors. To advance sea-ice model dynamics, one should carefully choose these parameters. But it also means that it is in principle possible to reproduce at least some LKF properties with currently available modeling techniques.

Model resolution, rheology, and solver accuracy have been reported before to affect the number of resolved LKFs (Girard et al., 2011; Rampal et al., 2016; Spreen et al., 2016; Q. Wang et al., 2016; Hutter et al., 2018; Bouchat & Tremblay, 2017; Koldunov et al., 2019; Rampal et al., 2019). Here, we find that the temporal resolution of the model (i.e. the time step) and the spatial resolution of the atmospheric forcing also have a strong impact on the spatial and temporal characteristics of resolved deformation features. The temporal resolution of the atmospheric forcing also affects the simulated LKF properties but with a lower impact. The dependence on the time step length may be related to the solver convergence, as shorter time steps imply smaller changes in external forcing between time levels and hence less work for the numerical solver.

From our analysis, it is not possible to unambiguously identify a single factor determining the accuracy of LKF representation in a model, because some factors only appear in combination. Still, our analysis suggests that a sea-ice model produces more realistic LKFs if the model configuration meets at least three of the following requirements: (1) time step smaller than 400 s, (2) grid spacing smaller than 5 km, (3) brittle visco-elastic rheology in combination with a Lagrangian grid, and (4) atmospheric forcing at resolutions smaller than 60 km. The number of ITD classes and the temporal resolution of the atmospheric forcing appear less important to explain the skill metrics scores. Thus, we recommend to choose the four parameters above with care when setting up sea ice simulations. Explicitly, models with a viscous-plastic rheology will always require very high grid resolution (see also Appendix A). The skill metrics defined in our study can be used as cost functions in systematic model parameter optimizations to quantify the observation-model misfit for LKF statistics. Based on our promising results for simulations with modified compressive and shear strength, we recommend to also consider the ellipse ratio e in such an optimization for (E)VP models.

SIREx is the first sea-ice model intercomparison effort that includes the main three rheologies employed in state-of-the-art sea-ice models. The (E)VP rheology, which is used in most, if not all, climate models, is well represented in our study with 30 out of 36 simulations. This emphasizes how important our findings for improving the representation of sea-ice conditions in climate projections. The MEB and EAP rheology, however, are each based on simulations of only one model code. For the MEB simulations, it is also not possible to cleanly disentangle whether it is the rheology alone or the combination with the Lagrangian grid that makes neXtSIM scoring higher than the average (E)VP model at the same resolution. A more different set of simulations or ideally a single modeling framework for all three rheologies would be required to unambiguously assess the effect of the rheology.

The combination of the deformation statistics from SIREx part I and the LKF statistics from SIREx part II shows that only the realism of deformation rate PDFs and spatial scaling analysis are correlated to LKF density skill metrics. This suggests that PDFs of deformation rates, which are relatively easy to compute, can be used to quickly assess sea-ice simulations, for instance during model tuning, before applying more sophisticated metrics such as the LKF statistics of part II or the scaling analysis of part I. There is, however, no clear correlation between the temporal multi-fractal scaling parameters and the LKF statistics, so that the scaling metrics of sea-ice deformation provide only some information on the number of deformation features, but that the feature-based evaluation of sea-ice deformation used in this study is required to deduce other properties of deformation features.

Finally, our feature-based evaluation of LKFs uses sea-ice deformation fields implicitly assuming that these deformation-field-based LKFs coincide with leads and pressure ridges. We find, however, that not all models develop the expected concentration and thickness anomalies along LKFs. In particular, the magnitude of these anomalies depends strongly on the model resolution. Only simulations with a resolution smaller than 2 km produce sea ice concentration down to 50 % in grid cells tagged as "leads". These differences due to model resolution could have a large impact on high-resolution coupled climate simulations to come, as ice-air-ocean interaction processes, such as heat flux or form drag and the extent to which they are resolved by an atmospheric model, depend fundamentally on the magnitude of the concentration and thickness along leads and pressure ridges. The evaluation of leads and pressure ridges as features of ice concentration and thickness fields will become feasible with increasing resolution of both simulations and satellite products. This will nicely complement the analysis of LKFs based exclusively on deformation data.

Appendix A Comparability of RGPS and model data

RGPS is a Lagrangian drift data set derived from SAR imagery. In the beginning of each winter, a network of virtual buoys is initialized on a regular grid with a grid spacing of 10km (in coastal regions 25km; Kwok, 1998). The position of each virtual buoy is updated every time a new SAR image is available which covers the position of this virtual buoy. The timing of the individual position record is different for all buoys, as they were covered by different or multiple overflights. On average the position of all buoys are updated every 3 days. Deformation rates are computed from the virtual buoy positions using line integral approximations. The temporal and spatial scales associated with this deformation rates vary due to the irregular temporal sampling and distortion of the cells caused by the advection. The average temporal and spatial scale is 3 days and 10 km. The Lagrangian deformation data is interpolated onto a regular grid with a spacing of 12.5km. This Eulerian deformation data set was used to derive the RGPS LKF data-set used in our analysis (Hutter et al., 2019).

The principle of computing deformation rates from tracked displacements has interesting consequences with respect to the resolution of deformation features that are resolved in the data. All displacements originating from fracture between two position records are recorded regardless their duration, as long as they exceed the spatial resolution of the SAR images, which is roughly 100 m. Therefore, the deformation features do not have a specific temporal resolution. The spatial resolution of the SAR images limits only the magnitude of the deformation rates (Lindsay et al., 2003), but not the width of the deformation features causing the deformation. In the context of model-observation comparisons, it is reasonable to choose the spatial resolution of LKFs referring to their minimal width. As a minimal width of LKFs can not be derived from RGPS, we refer to the RGPS data set having a 3-day temporal and 12.5 km spatial sampling rate, instead of using the term resolution.

The fact that the deformation derived from RGPS is not limited to a certain feature width nor a deformation duration time complicates the comparison with models that do not use a subgrid parameterisation of small-scale deformation, but explicitly resolve deformation features. In our comparison, these are all (E)VP, and EAP models. In those models, 6-10 grid cells are needed to resolve an LKF as a discontinuity in the concentration and thickness fields. Thus, the effective resolution of these simulations is accordingly larger than model's grid spacing. This explains in parts why the coarser resolution models in the comparison show fewer LKFs than RGPS (Fig. 1). Since the effective resolution has not been quantified, adapting of the model-observation analysis to the effective resolution in our analysis is not possible.

The spatial sampling of RGPS does not allow to distinguish if the recorded displacement is caused by one or multiple deformation features. Very high resolution models could resolve multiple deformation features within a 12.5×12.5 RGPS cell, which would distort the model-observation comparison of LKF numbers. The highest resolution models in our comparison, however, have a resolution of 1-2 km. Thus, their effective resolution is in the range of the spatial sampling rate of RGPS and we can exclude that this effect from affects our results.

The 3-day RGPS deformation rates can be seen as an "integral" of all deformation taking place within the 3-day sampling period of RGPS. We mimic this by filtering LKF pixels for each daily field and then combine three daily maps to a cumulative 3-day LKF map. Assuming that the exponential tail of the LKF lifetime distribution (Fig. 6) also holds for lifetimes smaller than 3 days, we potentially miss very short-lived LKFs in our model LKF data sets. However, LKFs are associated with strong velocity gradients and their signal are imprinted in the daily mean fields. In addition, forcing at very short temporal scale is needed to cause these short-lived deformations. Actually, we do not find differences in the deformation rate PDFs when using daily vs. hourly snapshot vs. mean

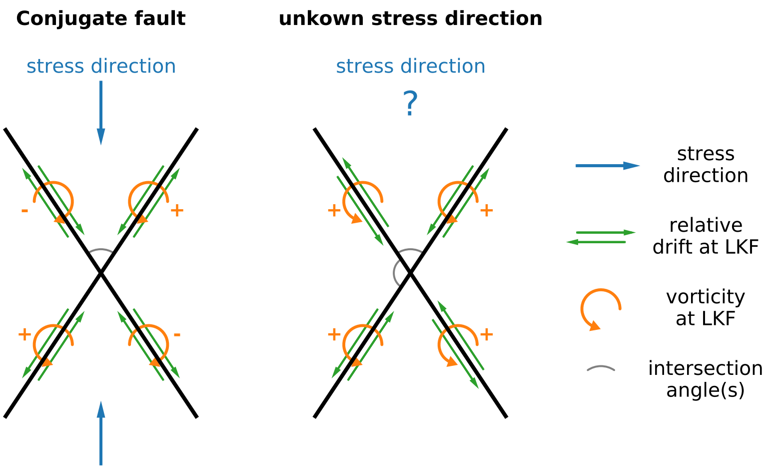

Figure B1. Schematic of relative displacement, vorticity, stress direction, and intersection angle along two intersection LKFs.

model diagnostics. Thus, we are confident that the different temporal sampling for models and RGPS does not have have a significant effect on our analysis. Very high frequency model output could be used to quantify this effect in a dedicated study.

Appendix B Principles of intersection angle selection

We study the intersection angle of LKFs, because it is directly related to the fracture angle for conjugate faults. The fracture angle is the angle between the LKF and the direction of the main stress, so therefore half of the intersection angle, and provide insights on the fracture physics. To compute the fracture angle, the direction of stress must be known. For RGPS and model simulations, however, only the drift and deformation data are provided. In our analysis, we use the vorticities derived from the relative displacement along two intersecting LKFs to determine the main direction of stress. The vorticity is computed from the sea-ice drift fields. The two LKFs of a conjugate fault have vorticities of opposite sign (Fig. B1). Thus, we label intersecting pairs of LKFs with vorticities of opposite sign as conjugate faults and compute the intersection angle relative to stress direction by measuring the angle from the LKF with positive vorticity to the LKF with negative vorticity. If both intersecting LKFs have vorticities of the same sign, it is not possible to determine the main stress direction causing the deformation. In this case, we take both possible intersection angles (angle measured from the LKF with positive vorticity to LKF with negative vorticity and vice versa) into account for the computation of the intersection angle PDF (Fig. 5).

Acknowledgments

Conceptualization, N.H. and A.B.; Methodology, N.H.; Resources, all authors; Data Curation, A.B.; Investigation, N.H.; Writing – Original Draft, N.H.; Writing – Review & Editing, all authors; Project administration, A.B. and N.H

D. Dukhovskoy was funded by the DOE (award DE-SC0014378) and HYCOM NOPP (award N00014-19-1-2674). The HYCOM-CICE simulations were supported by a grant of computer time from the DoD High-Performance Computing Modernization Program at NRL SSC. The daily fields from the 0.08 HYCOM-CICE experiment are available at the HYCOM data server `ftp://ftp.hycom.org/datasets/ARCc0.08/expt_11.0/data/` T. Rasmussen was funded by the Danish State through the National centre for Climate Research and by the SALIENSEAS project part of the ERA4CS programme, which is co-funded by the Innovation Fund Denmark and the Horizon 2020 Framework Programme of the European Union (Grant 690462). Q. Wang is supported by the German Helmholtz Climate Initiative REKLIM (Regional Climate Change). Data is available upon request. P. Myers was funded by the Natural Sciences and Engineering Research Council (NSERC) of Canada (RGPIN 04357 and RGPCC 433898). Experiments were run and are archived using facilities provided by Compute Canada (www.computecanada.ca). For more details on the ANHA configuration, visit http://knossos.eas.ualberta.ca/anha/anhatable.php. B. Tremblay was funded by the Natural Science and Engineering and Research Council (NSERC) Discovery Program and by the Environment and Climate Change Canada Grants & Contributions program.

Simulation data by the participating modeling groups is available upon request. The derived LKF data-sets will be archived and publicly available after the review and prior to publication.

References

Blockley, E., Vancoppenolle, M., Hunke, E., Bitz, C., Feltham, D., Lemieux, J.-F., ... Schroeder, D. (2020). The future of sea ice modeling: Where do we go from here? *Bulletin of the American Meteorological Society*, *101*(8), E1304 - E1311. Retrieved from `https://journals.ametsoc.org/view/journals/bams/101/8/bamsD200073.xml` doi: 10.1175/BAMS-D-20-0073.1

Bouchat, A., Hutter, N., & Tremblay, J. B. (2020). *Scaling and statistical properties of sea-ice deformation fields from models participating in the famos sea-ice rheology experiment.*

Bouchat, A., & Tremblay, B. (2017). Using sea-ice deformation fields to constrain the mechanical strength parameters of geophysical sea ice. *Journal of Geophysical Research: Oceans*, *122*(7), 5802–5825. Retrieved from `http://dx.doi.org/10.1002/2017JC013020` doi: 10.1002/2017JC013020

Bouchat, A., & Tremblay, B. (2019). *Reassessing the quality of sea-ice deformation estimates derived from the radarsat geophysical processor system and its impact on the spatio-temporal scaling statistics.* (*Submitted to the Journal of Geophysical Research: Oceans*)

Bouillon, S., & Rampal, P. (2015). Presentation of the dynamical core of neXtSIM, a new sea ice model. *Ocean Modelling*, *91*, 23 - 37. Retrieved from `http://www.sciencedirect.com/science/article/pii/S1463500315000694` doi: http://dx.doi.org/10.1016/j.ocemod.2015.04.005

Coon, M., Kwok, R., Levy, G., Pruis, M., Schreyer, H., & Sulsky, D. (2007). Arctic ice dynamics joint experiment (aidjex) assumptions revisited and found inadequate. *Journal of Geophysical Research: Oceans*, *112*(C11). Retrieved from `https://agupubs.onlinelibrary.wiley.com/doi/abs/10.1029/2005JC003393` doi: 10.1029/2005JC003393

Courtois, P., Hu, X., Pennelly, C., Spence, P., & Myers, P. G. (2017). Mixed layer depth calculation in deep convection regions in ocean numerical models. *Ocean Model.*, *120*, 60-78. doi: 10.1016/j.ocemod.2017.10.007

Cunningham, G. F., Kwok, R., & Banfield, J. (1994, Aug). Ice lead orientation characteristics in the winter beaufort sea. In *Proceedings of igarss '94 - 1994 ieee international geoscience and remote sensing symposium* (Vol. 3, p. 1747-1749 vol.3). doi: 10.1109/IGARSS.1994.399553

Dansereau, V., Weiss, J., Saramito, P., & Lattes, P. (2016). A Maxwell elasto-brittle rheology for sea ice modelling. *The Cryosphere*, *10*(3), 1339–1359. Retrieved from http://www.the-cryosphere.net/10/1339/2016/ doi: 10.5194/tc-10-1339-2016

Dempsey, J., Xie, Y., Adamson, R., & Farmer, D. (2012). Fracture of a ridged multi-year arctic sea ice floe. *Cold Regions Science and Technology*, *76-77*, 63 - 68. Retrieved from http://www.sciencedirect.com/science/article/pii/S0165232X11001947 (Max Coon Special issue) doi: https://doi.org/10.1016/j.coldregions.2011.09.012

Dukhovskoy, D. S., Yashayaev, I., Proshutinsky, A., Bamber, J. L., Bashmachnikov, I. L., Chassignet, E. P., ... Tedstone, A. J. (2019). Role of greenland freshwater anomaly in the recent freshening of the subpolar north atlantic. *Journal of Geophysical Research: Oceans*, *124*(5), 3333-3360. Retrieved from https://agupubs.onlinelibrary.wiley.com/doi/abs/10.1029/2018JC014686 doi: https://doi.org/10.1029/2018JC014686

Dupont, F., Higginson, S., Bourdallé-Badie, R., Lu, Y., Roy, F., Smith, G. C., ... Davidson, F. (2015). A high-resolution ocean and sea-ice modelling system for the Arctic and the North Atlantic oceans. *Geosci. Model Dev.*, *8*, 1577-1594. doi: 10.5194/gmd-8-1577-2015

Erlingsson, B. (1988). Two-dimensional deformation patterns in sea ice. *Journal of Glaciology*, *34*(118), 301–308.

Girard, L., Bouillon, S., Weiss, J., Amitrano, D., Fichefet, T., & Legat, V. (2011). A new modeling framework for sea-ice mechanics based on elasto-brittle rheology. *Annals of Glaciology*, *52*(57), 123-132. Retrieved from http://www.ingentaconnect.com/content/igsoc/agl/2011/00000052/00000057/art00017

Heorton, H. D. B. S., Feltham, D. L., & Tsamados, M. (2018). Stress and deformation characteristics of sea ice in a high-resolution, anisotropic sea ice model. *Philosophical Transactions of the Royal Society A: Mathematical, Physical and Engineering Sciences*, *376*(2129), 20170349. Retrieved from https://royalsocietypublishing.org/doi/abs/10.1098/rsta.2017.0349 doi: 10.1098/rsta.2017.0349

Hibler, W. D. (1979). A dynamic thermodynamic sea ice model. *J. Phys. Oceanogr.*, *9*, 815–846.

Hu, X., Sun, J., Chan, T., & Myers, P. G. (2018). Thermodynamic and dynamic ice thickness contributions in the Canadian Arctic Archipelago in NEMO-LIM2 numerical simulations. *The Cryosphere*, *12*, 1233-1247. doi: 10.5194/tc-12-1233-2018

Hunke, E., Allard, R., Blain, P., Blockley, E., Feltham, D., Fichefet, T., ... others (2020). Should sea-ice modeling tools designed for climate research be used for short-term forecasting? *Current Climate Change reports*, 1–16.

Hutchings, J. K., Heil, P., & Hibler, W. D. (2005). Modeling linear kinematic features in sea ice. *Monthly Weather Review*, *133*, 3481–3497. Retrieved from http://dx.doi.org/10.1175/MWR3045.1 doi: 10.1175/MWR3045.1

Hutter, N. (2015). *Viscous-plastic sea-ice models at very high resolution* (Master's Thesis, University of Bremen, Alfred Wegener Institute, Helmholtz Centre for Polar and Marine research). doi: 10013/epic.46129

Hutter, N. (2019). *lkf_tools: a code to detect and track Linear Kinematic Features (LKFs) in sea-ice deformation data (Version v1.0)* [code]. Zenodo. Retrieved from http://doi.org/10.5281/zenodo.2560078 (Zenodo) doi: 10.5281/zenodo.2560078

Hutter, N., & Losch, M. (2020). Feature-based comparison of sea ice deformation in lead-permitting sea ice simulations. *The Cryosphere*, *14*(1), 93–113. Retrieved from https://www.the-cryosphere.net/14/93/2020/ doi: 10.5194/tc-14-93

-2020

Hutter, N., Losch, M., & Menemenlis, D. (2018). Scaling properties of arctic sea ice deformation in a high-resolution viscous-plastic sea ice model and in satellite observations. *Journal of Geophysical Research: Oceans*, *123*(1), 672-687. doi: 10.1002/2017JC013119

Hutter, N., Zampieri, L., & Losch, M. (2019). Leads and ridges in Arctic sea ice from rgps data and a new tracking algorithm. *The Cryosphere*, *13*(2), 627–645. Retrieved from `https://www.the-cryosphere.net/13/627/2019/` doi: 10.5194/tc-13-627-2019

Hutter, N., Zampieri, L., & Losch, M. (2019). *Linear Kinematic Features (leads & pressure ridges) detected and tracked in RADARSAT Geophysical Processor system (RGPS) sea-ice deformation data from 1997 to 2008* [data set]. PANGAEA. Retrieved from `https://doi.org/10.1594/PANGAEA.898114` (Supplement to: Hutter, N et al. (2019): Leads and ridges in Arctic sea ice from RGPS data and a new tracking algorithm. The Cryosphere, https://doi.org/10.5194/tc-2018-207) doi: 10.1594/PANGAEA.898114

Koldunov, N. V., Danilov, S., Sidorenko, D., Hutter, N., Losch, M., Goessling, H., ... Jung, T. (2019). Fast EVP solutions in a high-resolution sea ice model. *Journal of Advances in Modeling Earth Systems*. Retrieved from `https://agupubs.onlinelibrary.wiley.com/doi/abs/10.1029/2018MS001485` doi: 10.1029/2018MS001485

Kwok, R. (1998). The RADARSAT geophysical processor system. In *Analysis of sar data of the Polar Oceans* (p. 235-257). Springer Berlin Heidelberg. Retrieved from `http://dx.doi.org/10.1007/978-3-642-60282-5\_11` doi: 10.1007/978-3-642-60282-5_11

Kwok, R. (2001). Deformation of the arctic ocean sea ice cover between november 1996 and april 1997: A qualitative survey. In J. Dempsey & H. Shen (Eds.), *Iutam symposium on scaling laws in ice mechanics and ice dynamics* (Vol. 94, p. 315-322). Springer Netherlands. Retrieved from `http://dx.doi.org/10.1007/978-94-015-9735-7\_26` doi: 10.1007/978-94-015-9735-7_26

Kwok, R., Hunke, E. C., Maslowski, W., Menemenlis, D., & Zhang, J. (2008). Variability of sea ice simulations assessed with RGPS kinematics. *Journal of Geophysical Research: Oceans*, *113*(C11), 1–20. Retrieved from `http://dx.doi.org/10.1029/2008JC004783` (C11012) doi: 10.1029/2008JC004783

Lemieux, J.-F., & Tremblay, B. (2009). Numerical convergence of viscous-plastic sea ice models. *Journal of Geophysical Research: Oceans*, *114*(C5). Retrieved from `https://agupubs.onlinelibrary.wiley.com/doi/abs/10.1029/2008JC005017` doi: https://doi.org/10.1029/2008JC005017

Lindsay, R. W., Zhang, J., & Rothrock, D. A. (2003). Sea-ice deformation rates from satellite measurements and in a model. *Atmosphere-Ocean*, *41*(1), 35-47. doi: 10.3137/ao.410103

Linow, S., & Dierking, W. (2017). Object-based detection of linear kinematic features in sea ice. *Remote Sensing*, *9*(5). Retrieved from `http://www.mdpi.com/2072-4292/9/5/493` doi: 10.3390/rs9050493

Losch, M., Fuchs, A., Lemieux, J.-F., & Vanselow, A. (2014). A parallel Jacobian-free Newton-Krylov solver for a coupled sea ice-ocean model. *Journal of Computational Physics*, *257, Part A*, 901–911. Retrieved from `http://www.sciencedirect.com/science/article/pii/S0021999113006402` doi: http://dx.doi.org/10.1016/j.jcp.2013.09.026

Lüpkes, C., Gryanik, V. M., Witha, B., Gryschka, M., Raasch, S., & Gollnik, T. (2008). Modeling convection over arctic leads with les and a non-eddy-resolving microscale model. *Journal of Geophysical Research: Oceans*, *113*(C9), 1–17. Retrieved from `http://dx.doi.org/10.1029/2007JC004099` (C09028) doi: 10.1029/2007JC004099

Madsen, K. S., Rasmussen, T. A. S., Ribergard, M. H., & Ringgaard, I. M. (2016).

High resolution sea ice modelling and validation of the arctic with focus on south greenlandic waters, 2004-2013. *Polarforschung*, *85*.

Mahoney, A. R., Eicken, H., Shapiro, L. H., Heinrichs, T., Meyer, F. J., & Gaylord, A. G. (2012). *Mapping and characterization of recurring spring leads and landfast ice in the beaufort and chukchi seas* [Report]. University of Alaska, Coastal Marine Institute. Retrieved from https://www.boem.gov/ESPIS/5/5226.pdf (Final Report: OCS Study BOEM 2012-067)

Marsan, D., Stern, H., Lindsay, R., & Weiss, J. (2004, Oct). Scale dependence and localization of the deformation of Arctic sea ice. *Phys. Rev. Lett.*, *93*, 178501. Retrieved from http://link.aps.org/doi/10.1103/PhysRevLett.93.178501 doi: 10.1103/PhysRevLett.93.178501

Marsan, D., Weiss, J., Métaxian, J.-P., Grangeon, J., Roux, P.-F., & Haapala, J. (2011). Low-frequency bursts of horizontally polarized waves in the arctic sea-ice cover. *Journal of Glaciology*, *57*(202), 231–237. doi: 10.3189/002214311796405834

Martin, T., Tsamados, M., Schroeder, D., & Feltham, D. L. (2016). The impact of variable sea ice roughness on changes in arctic ocean surface stress: A model study. *Journal of Geophysical Research: Oceans*, *121*(3), 1931-1952. Retrieved from https://agupubs.onlinelibrary.wiley.com/doi/abs/10.1002/2015JC011186 doi: https://doi.org/10.1002/2015JC011186

Mohammadi-Aragh, M., Goessling, H. F., Losch, M., Hutter, N., & Jung, T. (2018). Predictability of Arctic sea ice on weather time scales. *Scientific reports*, *8*.

Muilwijk, M., Ilicak, M., Cornish, S. B., Danilov, S., Gelderloos, R., Gerdes, R., ... Wang, Q. (2019). Arctic ocean response to greenland sea wind anomalies in a suite of model simulations. *Journal of Geophysical Research: Oceans*, *124*(8), 6286-6322. Retrieved from https://agupubs.onlinelibrary.wiley.com/doi/abs/10.1029/2019JC015101 doi: https://doi.org/10.1029/2019JC015101

Ólason, E. O., Rampal, P., & Dansereau, V. (2020). On the statistical properties of sea ice lead fraction and heat fluxes in the arctic. *The Cryosphere Discussions*, *2020*, 1–19. Retrieved from https://tc.copernicus.org/preprints/tc-2020-13/ doi: 10.5194/tc-2020-13

Proshutinsky, A., Krishfield, R., & Timmermans, M.-L. (2020). Introduction to special collection on arctic ocean modeling and observational synthesis (famos) 2: Beaufort gyre phenomenon. *Journal of Geophysical Research: Oceans*, *125*(2), e2019JC015400. Retrieved from https://agupubs.onlinelibrary.wiley.com/doi/abs/10.1029/2019JC015400 (e2019JC015400 2019JC015400) doi: https://doi.org/10.1029/2019JC015400

Rampal, P., Bouillon, S., Ólason, E., & Morlighem, M. (2016). nextsim: a new lagrangian sea ice model. *The Cryosphere*, *10*(3), 1055–1073. Retrieved from http://www.the-cryosphere.net/10/1055/2016/ doi: 10.5194/tc-10-1055-2016

Rampal, P., Dansereau, V., Olason, E., Bouillon, S., Williams, T., & Samaké, A. (2019). On the multi-fractal scaling properties of sea ice deformation. *The Cryosphere Discussions*, *2019*, 1–45. Retrieved from https://www.the-cryosphere-discuss.net/tc-2018-290/ doi: 10.5194/tc-2018-290

Ringeisen, D., Losch, M., Tremblay, L. B., & Hutter, N. (2019). Simulating intersection angles between conjugate faults in sea ice with different viscous–plastic rheologies. *The Cryosphere*, *13*(4), 1167–1186. Retrieved from https://www.the-cryosphere.net/13/1167/2019/ doi: 10.5194/tc-13-1167-2019

Ringeisen, D., Tremblay, L. B., & Losch, M. (2020). Non-normal flow rules affect fracture angles in sea ice viscous-plastic rheologies. *The Cryosphere Discussions*, *2020*, 1–24. Retrieved from https://tc.copernicus.org/preprints/tc-2020-153/ doi: 10.5194/tc-2020-153

Rothrock, D. A. (1975). The energetics of the plastic deformation of pack ice by ridging. *Journal of Geophysical Research*, *80*(33), 4514–4519. Retrieved from http://dx.doi.org/10.1029/JC080i033p04514 doi: 10.1029/JC080i033p04514

Schulson, E., Fortt, A., Iliescu, D., & Renshaw, C. (2006). On the role of frictional sliding in the compressive fracture of ice and granite: Terminal vs. post-terminal failure. *Acta Materialia*, *54*(15), 3923 - 3932. Retrieved from http://www.sciencedirect.com/science/article/pii/S1359645406003120 doi: https://doi.org/10.1016/j.actamat.2006.04.024

Schulson, E. M., & Hibler, W. D. (2004). Fracture of the winter sea ice cover on the Arctic ocean. *Comptes Rendus Physique*, *5*(7), 753 - 767. Retrieved from http://www.sciencedirect.com/science/article/pii/S1631070504001318 (Ice: from dislocations to icy satellites) doi: http://dx.doi.org/10.1016/j.crhy.2004.06.001

Spreen, G., Kwok, R., Menemenlis, D., & Nguyen, A. T. (2016). Sea ice deformation in a coupled ocean-sea ice model and in satellite remote sensing data. *The Cryosphere Discussions*, *2016*, 1–37. Retrieved from http://www.the-cryosphere-discuss.net/tc-2016-13/ doi: 10.5194/tc-2016-13

Stamoulis, C., & Dyer, I. (2000). Acoustically derived ice-fracture velocity in central arctic pack ice. *The Journal of the Acoustical Society of America*, *108*(1), 96-104. Retrieved from https://doi.org/10.1121/1.429448 doi: 10.1121/1.429448

Sumata, H., Kauker, F., Karcher, M., & Gerdes, R. (2019). Simultaneous parameter optimization of an arctic sea ice–ocean model by a genetic algorithm. *Monthly Weather Review*, *147*(6), 1899 - 1926. Retrieved from https://journals.ametsoc.org/view/journals/mwre/147/6/mwr-d-18-0360.1.xml doi: 10.1175/MWR-D-18-0360.1

Ungermann, M., Tremblay, L. B., Martin, T., & Losch, M. (2017). Impact of the ice strength formulation on the performance of a sea ice thickness distribution model in the arctic. *Journal of Geophysical Research: Oceans*. Retrieved from http://dx.doi.org/10.1002/2016JC012128 doi: 10.1002/2016JC012128

Walter, B. A., & Overland, J. E. (1993). The response of lead patterns in the Beaufort Sea to storm-scale wind forcing. *Annals of Glaciology*, *17*, 219–226. doi: 10.3189/S0260305500012878

Wang, K. (2007, 5). Observing the yield curve of compacted pack ice. *Journal of Geophysical Research: Oceans*, *112*(C5). Retrieved from https://doi.org/10.1029/2006JC003610 doi: 10.1029/2006JC003610

Wang, Q., Danilov, S., Jung, T., Kaleschke, L., & Wernecke, A. (2016). Sea ice leads in the arctic ocean: Model assessment, interannual variability and trends. *Geophysical Research Letters*, *43*(13), 7019–7027. Retrieved from http://dx.doi.org/10.1002/2016GL068696 doi: 10.1002/2016GL068696

Wang, Q., Koldunov, N. V., Danilov, S., Sidorenko, D., Wekerle, C., Scholz, P., ... Jung, T. (2020). Eddy kinetic energy in the arctic ocean from a global simulation with a 1-km arctic. *Geophysical Research Letters*, *47*(14), e2020GL088550. Retrieved from https://agupubs.onlinelibrary.wiley.com/doi/abs/10.1029/2020GL088550 (e2020GL088550 10.1029/2020GL088550) doi: https://doi.org/10.1029/2020GL088550

Wernecke, A., & Kaleschke, L. (2015). Lead detection in arctic sea ice from cryosat-2: quality assessment, lead area fraction and width distribution. *The Cryosphere*, *9*(5), 1955–1968. Retrieved from https://www.the-cryosphere.net/9/1955/2015/ doi: 10.5194/tc-9-1955-2015

Willmes, S., & Heinemann, G. (2016). Sea-ice wintertime lead frequencies and regional characteristics in the Arctic, 2003-2015. *Remote Sensing*, *8*(1). Retrieved from http://www.mdpi.com/2072-4292/8/1/4 doi: 10.3390/rs8010004